Inorganic Chemistry Communications 171 (2025) 113607

Contents lists available at ScienceDirect

Inorganic Chemistry Communications

journal homepage: www.elsevier.com/locate/inoche

A comprehensive analysis of structural, electronic, optical, mechanical, thermodynamic, and thermoelectric properties of direct band gap Sr_3BF_3 (B = As, Sb) photovoltaic compounds: DFT-GGA and mBJ approach

Muneef Hasan [a], Adil Hossain [a], Heider A. Abdulhussein [b,c], Abdullah Al Shadi [d], Bijoy Sorker [d], Ahmed Adnan Al-Khafagi [e], Redi Kristian Pingak [f], Diana Dahliah [g], Mohammed S. Abu-Jafar [g], Asif Hosen [a,*]

[a] Department of Materials Science and Engineering, Khulna University of Engineering & Technology (KUET), Khulna 9203, Bangladesh
[b] Department of Chemistry, Faculty of Science, University of Kufa, Najaf, Iraq
[c] College of Engineering, University of Warith Al-Anbiyaa, Kerbala, Iraq
[d] Department of Electrical and Electronic Engineering, Khulna University of Engineering & Technology (KUET), Khulna 9203, Bangladesh
[e] Al-Mustaqbal University, 51001 Babylon, Iraq
[f] Department of Physics, Faculty of Science and Engineering, The University of Nusa Cendana, Kupang 85001, Indonesia
[g] Department of Physics, An-Najah National University, Nablus, Palestine

ARTICLE INFO

Keywords:
DFT
Formation enthalpy
Tunable bandgap
Thermodynamic properties
Optoelectronic device

ABSTRACT

This study evaluates the physical properties of lead-free Sr_3BF_3 (B = As, Sb) photovoltaic compounds including structural, electronic, mechanical, optical, thermodynamic, and thermoelectric behavior using calculations based on DFT approach. Born stability criteria and formation enthalpy estimates show that the compounds under study are mechanically and thermodynamically stable. The initial lattice constants for Sr_3AsF_3 and Sr_3SbF_3 were determined to be 5.71 Å and 5.97 Å, respectively. While simulating the compounds under pressure, lattice constants, cell volumes, and bond lengths decrease. The band structure investigation shows that these compounds are semiconducting with an adjustable direct bandgap. The electronic band gap contracts by pressure, shifting the material from ultraviolet to the visible spectrum. This modification enhances electron transition from valence band maxima to conduction band minima, enhancing optical efficiency. The shift and rise in ductility and machinability index under pressure ensures good lubrication, low friction, and significant plastic deformation suitable for many industrial applications. Simultaneously, the static dielectric constant increases, increasing absorption and conductivity and red-shifting the optical spectrum, and reducing reflectivity in the visible spectrum. The thermodynamic behavior of the compounds was affected by both pressure and temperature variation. The thermoelectric figure of merit becomes closer to unity with a shorter band gap, indicating increased efficiency. Our findings suggest that Sr_3BF_3 (B = As, Sb) photovoltaic compounds could be used for the invention of next-generation solar cells and thermoelectric devices.

1. Introduction

There is a growing energy demand in modern times, driven by rapid population growth and rapid technological advancement. Finding renewable energy sources is essential to provide energy that meets demand and guarantees a steady supply. Among the most plentiful and reasonably priced sources of renewable energy available today is solar energy. However, conventional Materials for solar cells, such as Silicon (Si), GaAs, CdTe, CIGS, Sb_2Se_3, CMTS, and $FeSi_2$ have been showing little to none advancements in the field of photovoltaics [1–3]. Materials like Si have little potential for improvement because of their indirect and inefficient bandgaps, as well as their highly costly manufacturing processes [4]. Perovskite-derived materials have great promise in solar cell technology due to their wide variety of advantageous features, which makes them highly appealing [5]. When the thickness of the layer of perovskite-derived materials is less than 1 μm exceeds other semiconductor materials in terms of photon capture capabilities [6]. Perovskite-derived inorganic materials exhibit remarkable optical and

* Corresponding author.
E-mail addresses: haydera.abdulhussein@uokufa.edu.iq (H.A. Abdulhussein), asif@mse.kuet.ac.bd (A. Hosen).

https://doi.org/10.1016/j.inoche.2024.113607
Received 16 September 2024; Received in revised form 15 November 2024; Accepted 18 November 2024
Available online 22 November 2024

electrical qualities, which make them extremely appealing for the making of next-generation PV cells [7]. Inorganic perovskite-based materials are frequently synthesized for diverse applications in the realms of photoelectricity and other energy-related disciplines [8]. Efficiency of power conversion (PCE) of perovskite-derived materials in solar cells which were 3.8 % in 2009, have greatly increased [9] to the current global record of 25.7 % as of 2022 [10]. Also, Perovskite-derived materials have made substantial advancements in their properties during the past decade, which has driven their growth [11]. Regrettably, these materials' long-term durability in actual environments will be greatly affected by their high sensitivity to moisture, wind, sunshine, and temperature [12]. The hysteresis effect, which causes instability and erratic findings when measuring conditions change, is another drawback to using these devices [8]. The sustainability of solar cells based on perovskite-like materials is additionally hindered by the existence of lead, which poses serious concerns for human health and the environment during both production and disposal [12]. Hence, it is important to research IHP materials that are both highly efficient as well as economically feasible to accelerate the growth of the solar cell industry.

Perovskite derived materials of the A_3BX_3 type are inorganic and feature a particular crystal structure in which X is an anion, A is a large cation, and B is a smaller cation. By altering the cation or halide atom (A, B, or X-site), perovskite-like A_3BX_3 structure features like performance characteristics [13] can be modified in response to hydrostatic pressure [14–16]. The exceptional properties of perovskite-derived materials with an A_3BX_3 structural arrangement such as their direct bandgap material, high electrical qualities, mechanical stability, and lack of lead make them highly sought-after [16–18]. The structural advantages allow A_3BX_3 compounds to attain desirable physical properties by undergoing externally applied hydrostatic pressure. DFT-based simulations give us a glimpse of their projected change due to pressure. Recent studies by S. Joifullah et al. [19] of Sr_3PX_3 (X = Cl, Br) and Md. Adil et al. [20] of Ca_3MF_3 (M = As, Sb) and Sr_3ZBr_3 (Z = As, Sb) [21] compounds showed the pressure-dependent changes of perovskite-derived A_3BX_3 structure which were both intriguing and thought-provoking. They found that under high pressure, the perovskite undergoes a transition to a metallic state. This discovery highlights its potential application scenario in solar energy systems, as it exhibits both mechanical resilience and improved optoelectronic properties.

According to our knowledge, there is no previous pressure-induced investigation of Sr_3BF_3 (B = As, Sb) photovoltaic compounds. Previously, studies conducted by Ali Algahtani et al. [22] and Ghosh et al. [23] show the possibility of Sr_3AsF_3 for application to solar cells. Hence, conducting a thorough investigation of Sr_3BF_3 (B = As, Sb) compounds is essential for the development of devices that both use electrical and optoelectronic technologies. This research aims to apply first-principles density functional theory. (FP-DFT) computations to look into the structural, mechanical, optical, and electronic properties of Sr_3BF_3 under situations of stress between 0 and 30 GPa. Additionally, the thermodynamic and thermoelectric behaviors of these compounds as a function of temperature were revealed in this work to identify any favorable characteristics. Hence, conducting this study will yield advantages in identifying the particular traits of Sr_3BF_3 (B = As, Sb) photovoltaic compounds and their usefulness in advanced solar cells and photovoltaic systems.

2. Computational details

The computations were implemented using the plane-wave basis set of the Quantum ESPRESSO approach, which is reliant upon the Density Functional Theory (DFT) [24,25]. We have employed the Perdew–Burke–Ernzerhof (GGA-PBE) approach [26], which is a generalized gradient approximation (GGA) that incorporates exchange–correlation functional, used in our computations. The interaction between electrons and ions was simulated using ultrasoft pseudopotentials [27,28] of the PBE type for the elements Sr, As, Sb, and F. At first, the structures were optimized by adjusting their volume and geometry to achieve the most advantageous lattice constants and atomic positions. The BFGS (Broyden-Fletcher-Goldfarb-Shanno) quasi-Newton methodology was implemented to execute a comprehensive structural relaxation, leading to the complete optimization of atom locations [29]. The wave function was defined by the threshold energy. established at 40 Rydberg, whereas the charge density's threshold energy was established at 440 Rydberg. The Brillouin Zone was sampled utilizing a Monkhorst-Pack grid consisting of a 7 × 7 × 7 arrangement of the K-point meshes. The calculations were performed with a force convergence threshold of 10^{-3} eV/Å and an energy convergence threshold of 10^{-6} eV. GGA is recognized for its tendency to underestimate the band gap, particularly in materials with d or f-electron. In the Wien2k code [30], the Tran-Blaha modified Becke-Johnson (TB-mBJ) approximation [31] is also employed to evaluate electronic characteristics as it provides more accurate band gap estimations in semiconductors and insulators. To accomplish charge and energy convergence, we used a linearized augmented plane-wave basis set with $l_{max} = 10$ and $R_{MT}K_{max} = 7$ (K_{max} is the maximum K-value). VESTA program was utilized to present the optimized structure of both materials [32]. The elastic constants for the present experiment were determined by employing the formula of the Thermo-PW package, which is employed to ascertain the mechanical properties. The ELATE code [33] was employed to depict Young's modulus, bulk modulus, and shear modulus in a three-dimensional format. We have employed first-order time-dependent perturbation theory in investigating the optical properties of material formation and analyzing its dynamic stability [34,35]. Optical absorption coefficients are primarily correlated with the complex dielectric function. The equation can be expressed as $\varepsilon(\omega) = \varepsilon_1(\omega) + j\varepsilon_2(\omega)$. Additionally, we estimated thermodynamic parameters using a quasi-harmonic Debye model with the Gibbs2 package [36] and used the semi-classical Boltzmann-based BoltzTrap package [37] to study thermoelectric characteristics.

3. Results and discussion

3.1. Structural properties

Inorganic compounds without lead like Sr_3BF_3 (B = As, Sb) crystallize in space group *Pm-3m* (221) [38]. Seven atoms make up the unit cell: 3Sr, 1B (B = As, Sb), and 3F atoms. Here, the B atoms are located at the coordinates (0, 0, 0) and occupy the 1a Wyckoff position., F atoms are arranged evenly throughout (0, 0.5, 0.5) fractional coordinates featuring a 3c Wyckoff position within a unit cell and Sr atoms are positioned at fractional coordinates of (0.5, 0, 0) within the Wyckoff site 3d. This optimized crystal structure is depicted in Fig. 1. The optimized lattice parameter, along with other ground state properties, is displayed in Table 1. The structural stability of the compounds is verified using the Goldschmidt tolerance factor. It is represented as [39]:

$$t = \frac{r_A + r_X}{\sqrt{2}(r_B + r_X)} \quad (1)$$

From Table 1, the tolerance factor values that have been calculated fall within the range of 0.813–1.059 demonstrating stability [40]. Fig. 2 displays the changes in total energy concerning volume. It is seen that the minimum energy values are −378.018 and −377.333 Ry, corresponding to the ground state volumes of 185.76 and 213.08 $Å^3$ for Sr_3AsF_3 and Sr_3SbF_3, respectively. Therefore, the computed lattice parameters for Sr_3AsF_3 was found to be 5.71 Å which closely aligns with the previous research 5.77 [21], and 5.62 [22], and computed lattice parameter for Sr_3SbF_3 was found 5.97 Å. Regrettably, the compounds Sr_3SbF_3 (B = As, Sb) have not been synthesized through experimentation. Consequently, we are unable to contrast the results of our calculations with any existing experimental reports. Fig. 3 illustrates the impact of hydrostatic pressure (which varied from 0 to 30 GPa) on the volume and lattice constant of the unit cell. Both compounds exhibit a reduction in unit cell volume and lattice constant as the hydrostatic

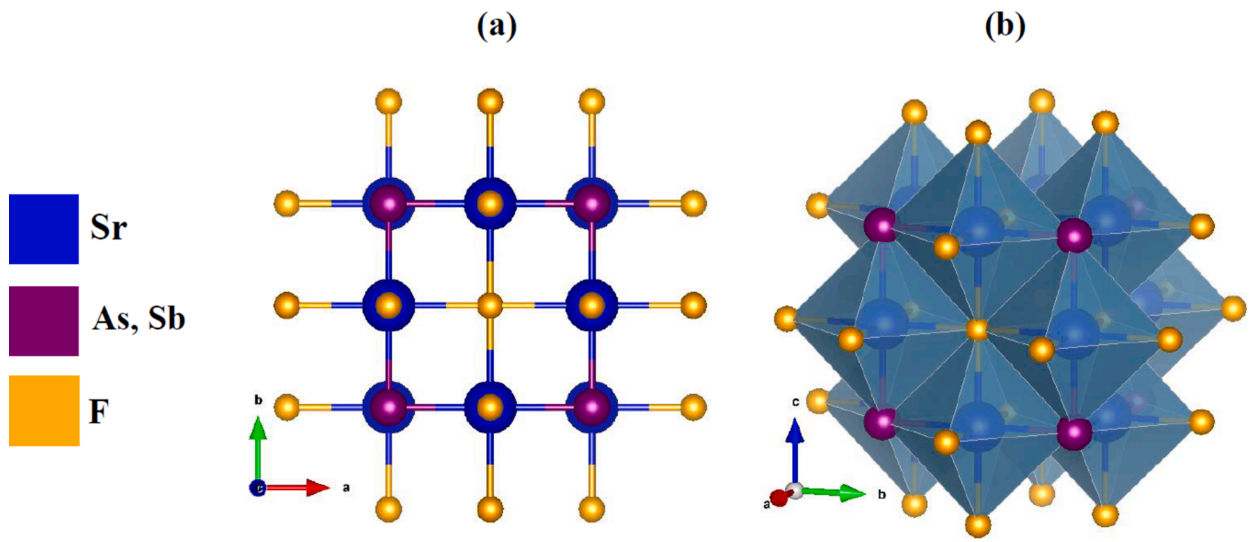

Fig. 1. (a) 2D and (b) 3D optimized crystal structure of Sr_3BF_3 (B = As, Sb).

Table 1
Ground state parameters of the unit cell and band gap for cubic compounds Sr_3BF_3 (B = As, Sb).

Optimized Structural Parameters	Sr_3AsF_3	Other Cal.	Sr_3SbF_3
Lattice constant (a_0) in Å	5.71	5.77 [22] 5.62 [23]	5.97
Optimum volume V_0 in $Å^3$	185.76		213.08
Bulk modulus (B) in GPa	30.04		35.59
Pressure derivative of bulk modulus (B')	4.17		3.71
Ground state energy (E_0) in Ry	−378.018		−377.333
Tolerance factor (t_0)	0.932		0.851
Band Gap (E_g) in eV	$3.26^{TB\text{-}mBJ}$ $1.60^{GGA\text{-}PBE}$	1.60^{PBE} [22] 1.68^{PBE} [23]	$2.95^{TB\text{-}mBJ}$ $1.69^{GGA\text{-}PBE}$

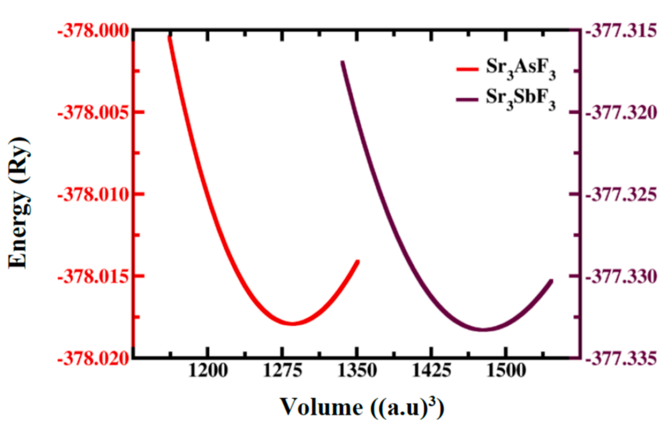

Fig. 2. Total energy with respect to volume curve for Sr_3AsF_3 and Sr_3SbF_3.

pressure is raised (Table 2). Conversely, when the volume decreases, the density increases in correlation given the increase in pressure (Table 6). This phenomenon can be attributed to the shortening of the bond, as outlined in (Table 3), indicating a reduction in the atomic distance. This can contribute to a reduction in the energy difference between the valence and conduction bands (band gap) and the occurrence of atomic orbital overlapping.

The energy of formation ΔE_f of both the compounds has been determined to evaluate their chemical and thermodynamic stability, employing the given equation:

$$\Delta E_f(Sr_3BF_3) = \frac{[E_{tot.}(Sr_3BF_3) - 3E(Sr) - E(B) - 3E(F)]}{N} \quad (2)$$

According to Table 2, the formation energy of the Sr_3SbF_3 (B = As, Sb) compounds is consistently negative at all applied pressures. This implies that the compounds are chemically and thermodynamically stable under all applied pressures [41,42]. Therefore, it may be deduced that they can be achieved through experimental means in both normal and pressured environments.

3.2. Phonon stability

The phonon dispersion analysis of a material gives us an idea about the stability of crystal structures, thermal, mechanical, vibrational, and electronic properties. For phonon dispersion analysis of Sr_3SbF_3 (B = As, Sb) compounds we have constructed a 3 × 3 × 3 supercell to encompass a wider range of vibrational modes and atomic interactions and using a q-vector grid of 4 × 4 × 4 for reciprocal space sampling. Phonon dispersion graphs at 0 GPa of both compounds are mapped out in Fig. 4 which shows no negative frequencies. This conforms to the criteria of dynamic stability of the materials [43,44]. The previous study carried out by Ghosh et al. [23] also validated the dynamic stability of Sr_3AsF_3. There are some similarities for both Sr_3AsF_3 and Sr_3SbF_3 compounds in the phonon dispersion graphs along the X–R–M–Γ–R high symmetry points with notable dips at Γ high symmetry point for both compounds. As we increase the given pressure to 30 GPa, we can see that negative frequencies in the phonon curve emerge. From this point of view our compounds become dynamically unstable. However, the elastic properties calculated from mechanical stability analysis show the compounds are mechanically stable. So, a general perception is that a metastable state exists if the compound is dynamically unstable but mechanically stable [45].

3.3. Electronic properties

The phrase "electronic properties" refers to distinct qualities also the behavior of a compound which are connected to the concept of motion and arrangement in its crystalline or molecular structure due to the presence of electrons. Analyzing electronic features, such as the structure of the bands and the density of the states, is vital for having a deeper understanding of optical properties. Band structures of Sr_3AsF_3 and Sr_3SbF_3 compounds were assessed under varying hydrostatic pressures. employing the GGA-PBE and TB-mBJ functionals within the Brillouin

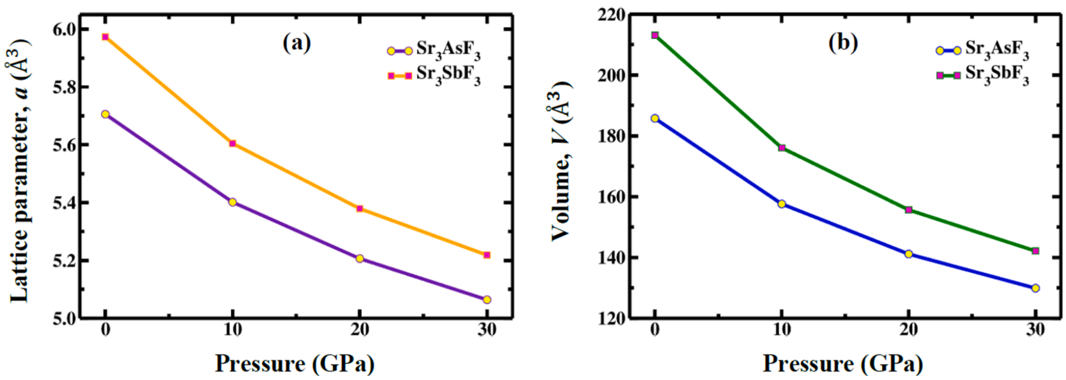

Fig. 3. Effect of pressure on (a) lattice constant and (b) unit cell volume of Sr_3BF_3 (B = As, Sb) compounds.

Table 2
Calculated values of unit cell volume (V), lattice constant (a), formation energy (E_f) and band gap (E_g) of Sr_3BF_3 (B = As, Sb) compounds from 0 to 30 GPa pressure.

Phase	Compound	Calculated data		Pressure (GPa)			
				0	10	20	30
Cubic (Pm3m)	Sr_3AsF_3	a (Å)		5.71	5.40	5.21	5.06
		V (Å^3)		185.76	157.60	141.12	129.87
		E_f (eV)		−4.93	−3.39	−2.07	−0.86
		E_g (eV)	TB-mBJ	3.26	2.59	1.98	1.36
			GGA-PBE	1.60	1.34	0.76	0.23
	Sr_3SbF_3	a (Å)		5.97	5.60	5.38	5.22
		V (Å^3)		213.08	176.06	155.65	142.11
		E_f (eV)		−4.55	−2.82	−1.35	−0.03
		E_g (eV)	TB-mBJ	2.95	2.21	1.62	0.99
			GGA-PBE	1.69	1.28	0.64	0.05

Table 3
Calculated bond length of Sr_3BF_3 (B = As, Sb) cubic compounds under various applied pressures.

Pressure (GPa)	Bond length (Å)					
	Sr_3AsF_3			Sr_3SbF_3		
	Sr-As	As-F	Sr-F	Sr-Sb	Sb-F	Sr-F
0	2.85	4.03	2.85	2.98	4.22	2.99
10	2.70	3.82	2.70	2.80	3.96	2.80
20	2.60	3.68	2.60	2.69	3.80	2.69
30	2.53	3.58	2.53	2.61	3.69	2.61

zone range X–R–M–Γ–R and demonstrated in Figs. 5–8 respectively. In this study, the TB-mBJ approximation [31] is employed in addition to GGA-PBE [26] so as to acquire a more accurate calculation of the spacing between the electronic band gaps of the photovoltaic materials as GGA-PBE tends to underestimate it. TB-mBJ is an altered variation of the exchange–correlation potential that Becke and Johnson proposed. The degeneracy of some states is eliminated by TB-mBJ approximation from GGA-PBE approximation. TB-mBJ is a semi-local exchange potential that closely resembles the behavior of orbital-dependent potentials, resulting in calculations that are only marginally more expensive than GGA calculations. Consequently, it can be implemented in an effective manner on larger systems [46]. In the band structure plot, the Fermi level (E_F) is denoted by a horizontal dashed line located along 0 eV. The two bands: the valence band (VB) and the conduction band (CB), are represented by line segments that are colored and are positioned below and above the E_F, accordingly. According to semiconductor theory, understanding the material's band structure surrounding the Fermi level (E_F) is crucial for knowing its physical characteristics. Thus, we have demonstrated the band structure within the −6 to 6 eV energy range surrounding the Fermi level. Both compounds display the maximum of the valence band (VBM) and the lowest of the conduction band (CBM) occurring at the Γ-point of the Brillouin zone when the pressure is 0 GPa. Therefore, Sr_3AsF_3 and Sr_3SbF_3 have a band gap (E_g) of 1.60 and 1.69 eV respectively, which are direct in nature, as determined using GGA-PBE functional. The band gap of Sr_3AsF_3 using GGA-PBE scheme is comparable to what found in previous studies 1.60 [21] and 1.68 [22]. The band gap values obtained using TB-mBJ approximation are around 3.26 eV and 2.95 eV, respectively. As the applied pressures increase, CBM of both compounds moves closer to the Fermi level (E_F), causing a decrease in value of the valance band and conduction band gap (E_g) as illustrated in Figs. 5–8. Fig. 9 illustrates a graphical demonstration of the decrease in E_g for both compounds when subjected to external pressure. All the values found for E_g for different pressures are tabulated in Table 2. At ambient pressure, both compounds possess a higher band gap value than the pressure-induced system. When the pressure from external forces rises, the band gap of both compounds decreases linearly. Applying a hydrostatic pressure of 30 GPa caused the bandgap of Sr_3AsF_3 to decrease from 1.60 to 0.23 eV for GGA-PBE as well as from 3.26 eV to 1.36 eV, when TB-mBJ functional was utilized, while for Sr_3SbF_3, the bandgap decreased from 1.69 to 0.05 eV for GGA-PBE also from 2.95 eV to 0.99 eV when TB-mBJ functional was employed. It has been demonstrated in previous studies that the band gap is negatively correlated with external pressure [47,48]. Throughout the entire pressure-induced process, both Sr_3AsF_3 and Sr_3SbF_3 maintained their direct bandgap electronic structure. The decrease in E_g for both compounds facilitate the quicker and more rapid transfer of electrons to the conduction band of electrons moving from the valence band, which may enhance the optical properties by allowing the compounds to respond to a photon energy across a wider spectrum. These aforementioned features enable the materials to be particularly attractive for optoelectronic device applications [49,50].

Fig. 10(a) and (b) illustrate the total density of states (TDOS) of Sr_3AsF_3 as well as Sr_3SbF_3, respectively, at varying hydrostatic pressures up to 30 GPa utilizing the TB-mBJ and GGA-PBE approximations. Both compounds demonstrate a significant pressure-induced impact on the

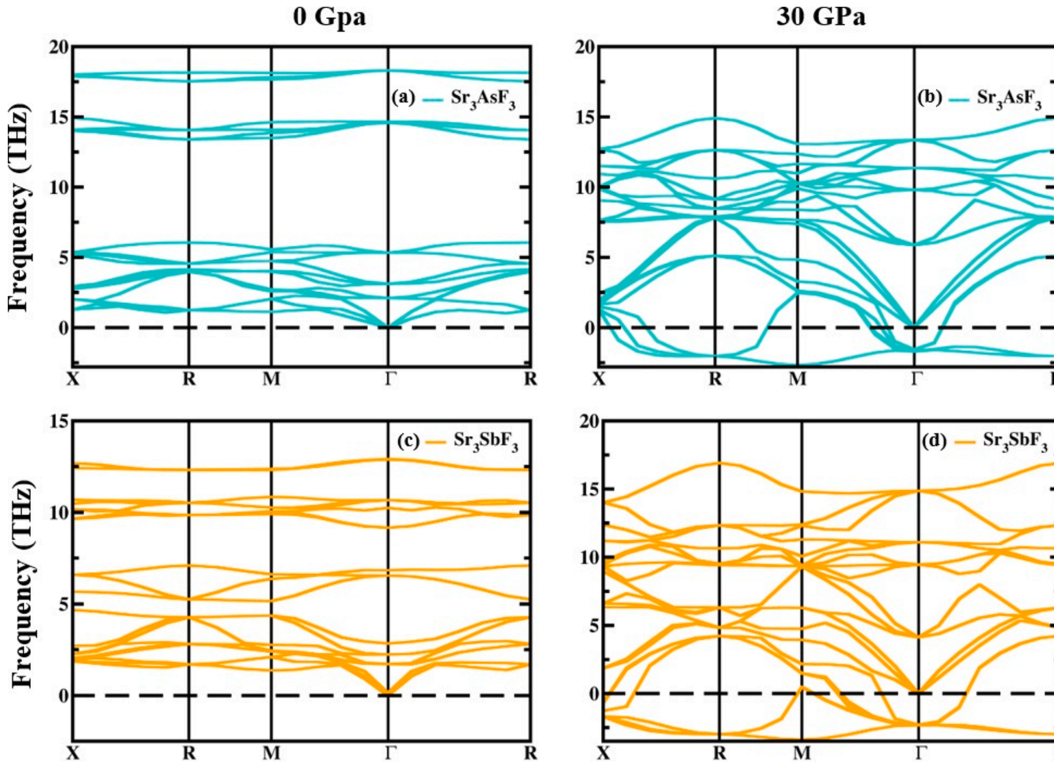

Fig. 4. Phonon dispersion spectrum of (a) Sr_3AsF_3 and (b) Sr_3SbF_3 under 0 GPa and 30 GPa pressure.

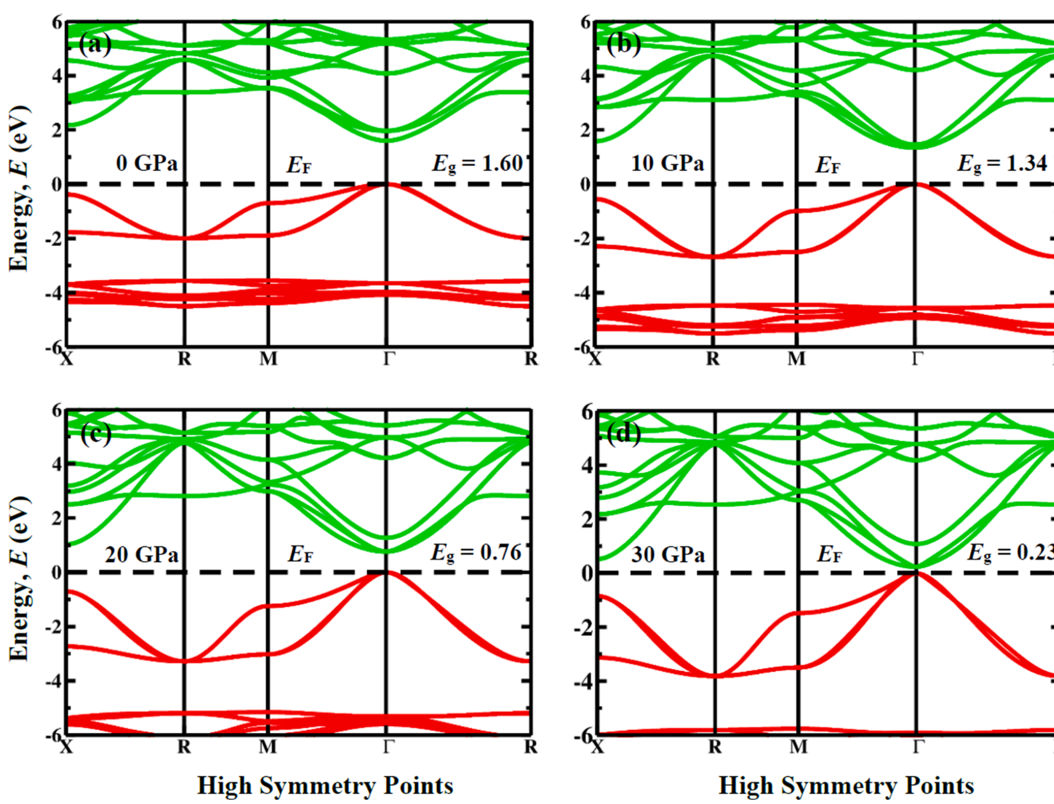

Fig. 5. Influence of pressure on band structure of Sr_3AsF_3 at (a) 0 GPa, (b) 10 GPa, (c) 20 GPa, and (d) 30 GPa via GGA-PBE approximation.

total density of states (TDOS) within the band of conduction. The total density of states (TDOS) peaks of both compounds approach the Fermi energy level (E_F) with rising pressure. Peak shifting, when exposed to pressure, results in a narrower band. This occurrence can also be seen in the band structures of the compounds.

The computation of Partial Density of States (PDOS) is essential to

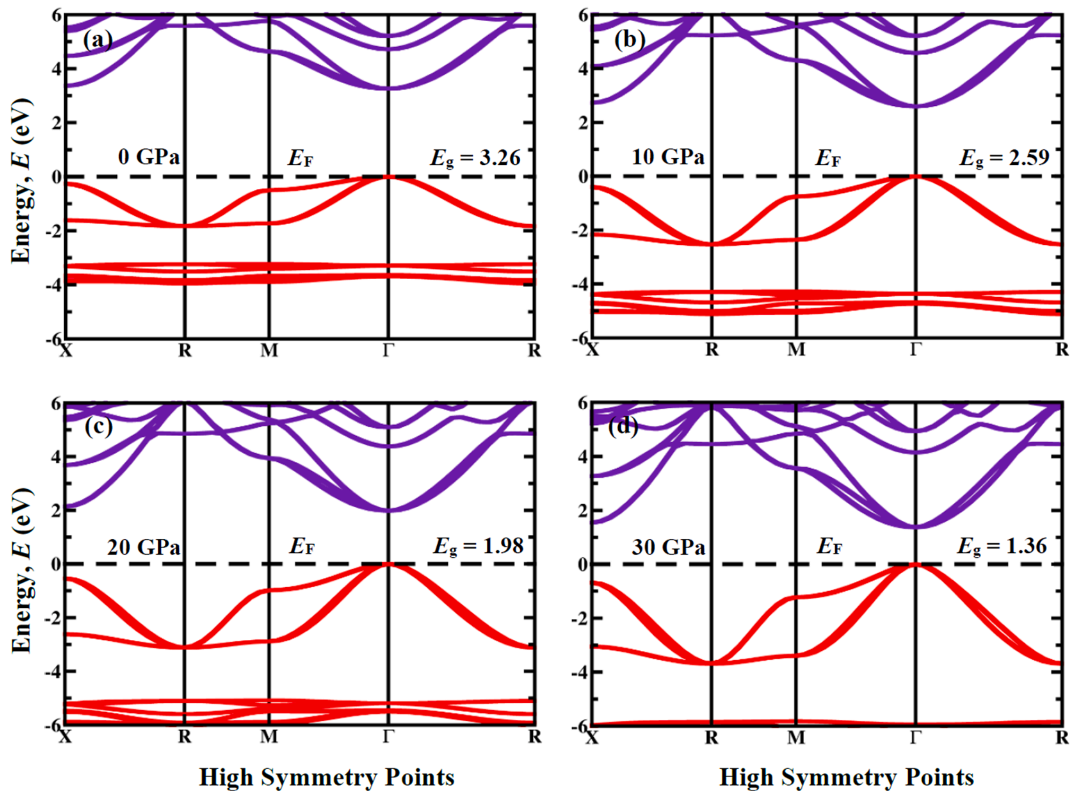

Fig. 6. Influence of pressure on band structure of Sr_3AsF_3 at (a) 0 GPa, (b) 10 GPa, (c) 20 GPa, and (d) 30 GPa via TB-mBJ approximation.

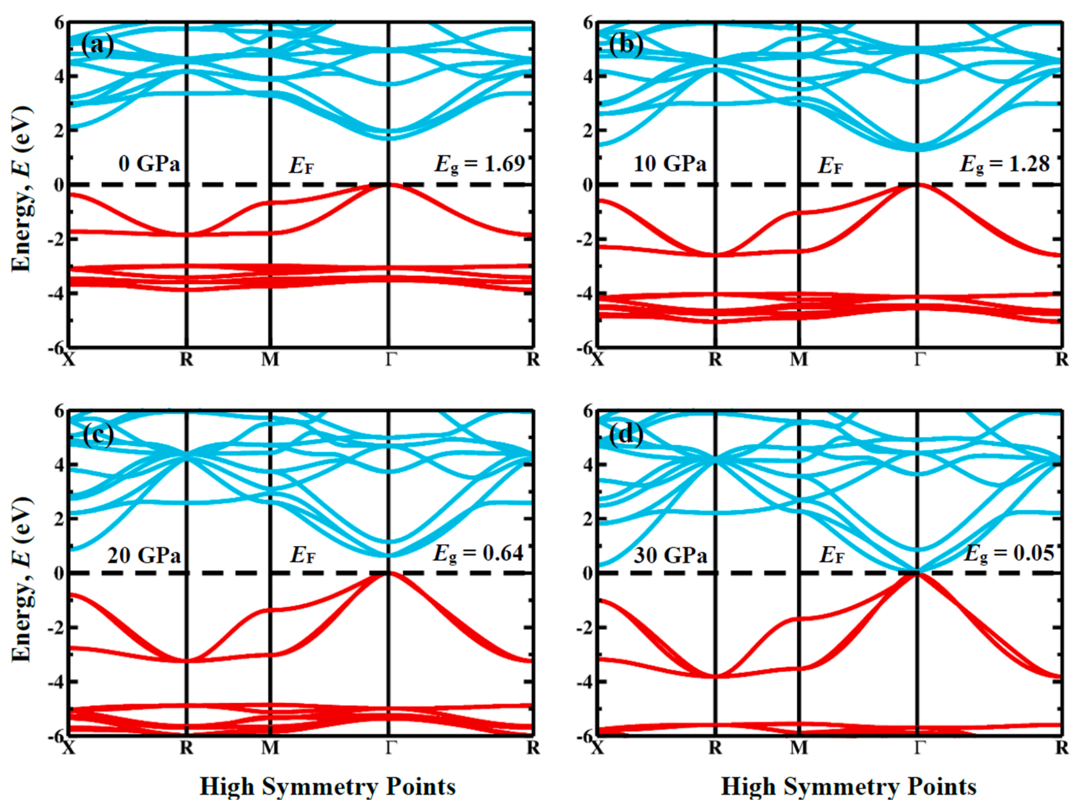

Fig. 7. Influence of pressure on band structure of Sr_3SbF_3 at (a) 0 GPa, (b) 10 GPa, (c) 20 GPa, and (d) 30 GPa via GGA-PBE approximation.

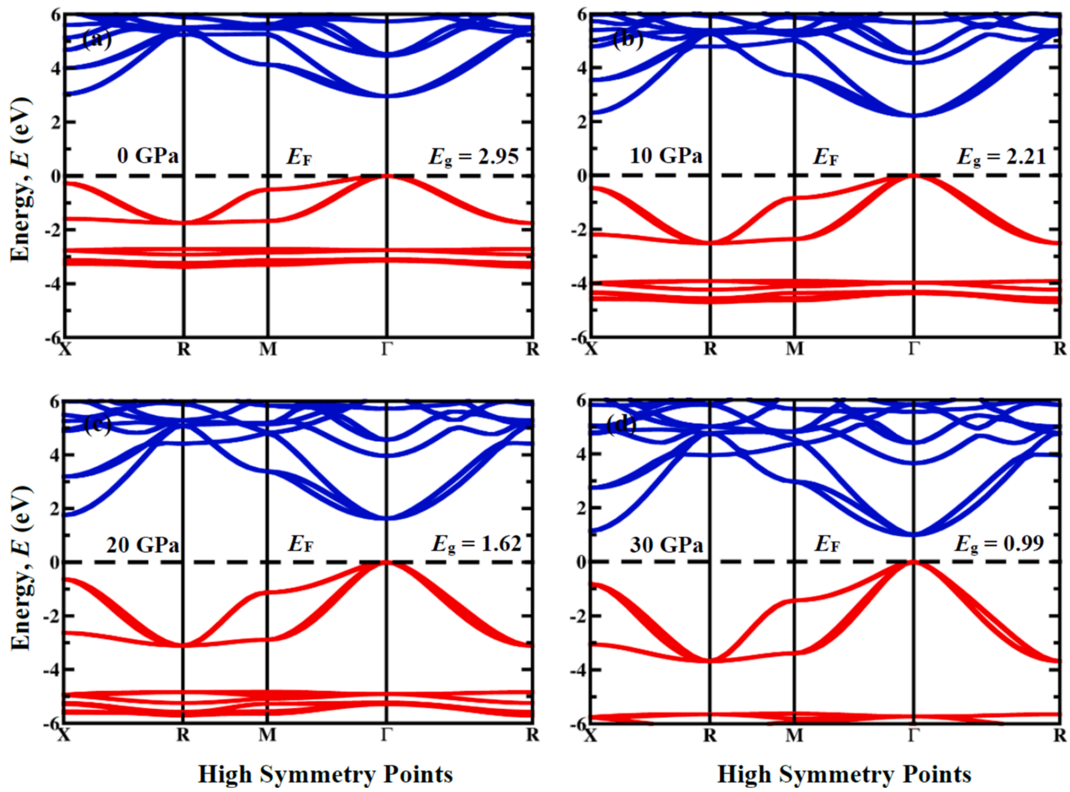

Fig. 8. Influence of pressure on band structure of Sr_3SbF_3 at (a) 0 GPa, (b) 10 GPa, (c) 20 GPa, and (d) 30 GPa via TB-mBJ approximation.

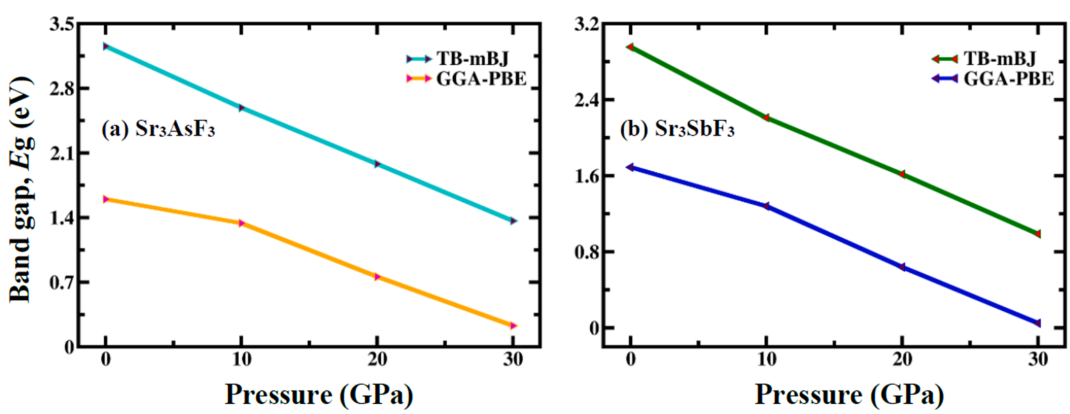

Fig. 9. Narrowing of bandgap energy of (a) Sr_3AsF_3 and (b) Sr_3SbF_3 with increasing pressure from 0 to 30 GPa.

discern the precise atomic contributions on the band structure of a material. Figs. 11 and 12 illustrate the Partial Density of States (PDOS) for Sr_3AsF_3 and Sr_3SbF_3 photovoltaic compounds, respectively. The PDOS is shown at different hydrostatic pressures, covering an energy range of −6 eV to 6 eV. The majority of the valence band at the Fermi level primarily originates from As-4p (Sb-5p) and F-2p orbitals. There is also little contribution from the Sr-4p and Sr-5s orbitals for both compounds. At a pressure of 30 GPa, the contribution of the As-4p orbital becomes prominent in Sr_3AsF_3, whereas the contribution of the Sb-5p orbital in Sr_3SbF_3. In contrast, the conduction band of both compounds predominantly results from the Sr-4p and Sr-5s orbitals, either under different hydrostatic pressures or at zero hydrostatic pressure. In addition to the Sr-4p and Sr-5s orbitals, we have found small contributions from the F-2s and F-2p orbitals in both Sr_3AsF_3 and Sr_3SbF_3 compounds. The narrowing of the E_g can be attributed mostly to the Sr-4p and Sr-5s orbitals in both compounds in CB as the orbitals move towards E_F upon the use of hydrostatic pressure. This phenomenon can be credited to the increased hybridization happening between the As-4p (Sb-5p) and Sr-4p orbitals. Furthermore, the decrease in bond length caused by pressure (as seen in Table 3) could promote the merging of As-4p (Sb-5p) and Sr-4p electronic orbitals located within the conduction band (CB).

3.4. Mechanical properties

The evaluation of the structural integrity of a material and its mechanical qualities relies significantly on the elastic constants (C_{ij}) [51]. Elastic characteristics refer to the capability of a material to undergo plastic deformation under tensile stress and thereafter recover its initial shape upon stress removal. These properties offer significant information regarding the bonding that occurs between adjoining atomic planes, the degree of anisotropy, and the stability of the structure [52]. Cubic materials possess three independent elastic constants: C_{11}, C_{12}, and C_{44}. Table 4 shows the computed values of C_{11}, C_{12}, and C_{44} of Sr_3BF_3 (B =

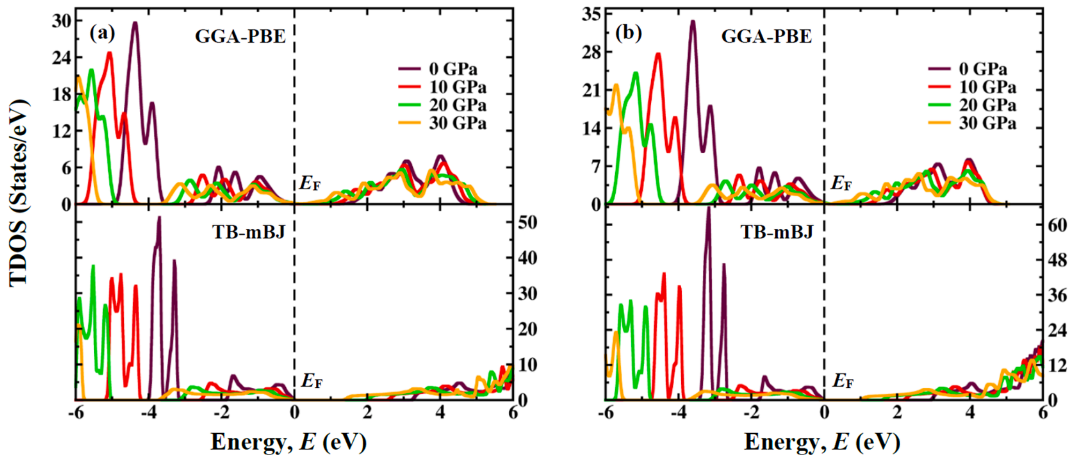

Fig. 10. The determined total density of states (TDOS) via TB-mBJ and GGA-PBE scheme of (a) Sr_3AsF_3 and (b) Sr_3SbF_3 under hydrostatic pressure 0 to 30 GPa.

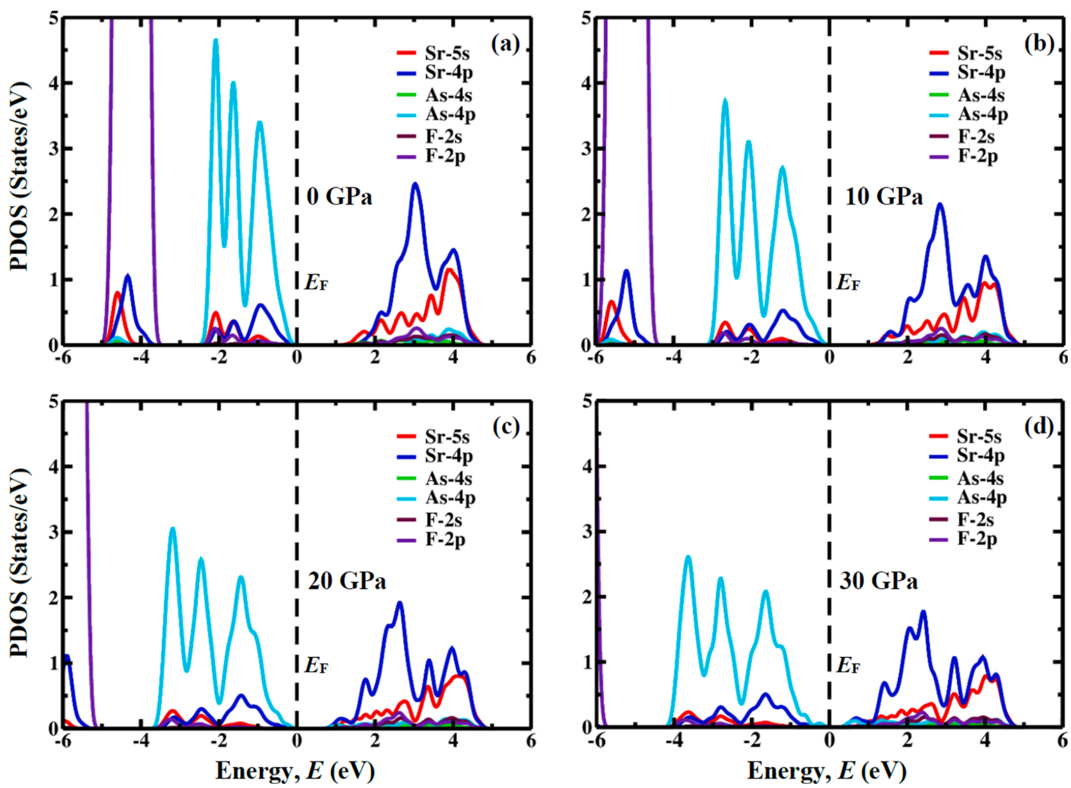

Fig. 11. Calculated partial density of states (PDOS) of Sr_3AsF_3 under different applied pressures.

As, Sb) photovoltaic compounds under hydrostatic pressure. The calculated values of C_{11}, C_{12}, and C_{44} of Sr_3AsF_3 at 0 GPa pressure are 82.71, 12.03, 19.70 respectively. This aligns with the findings in previous works: $C_{11} = 81.81$, $C_{12} = 12.24$, and $C_{44} = 19.05$ [21] and $C_{11} = 86.05$, $C_{12} = 15.08$, and $C_{44} = 19.83$ [22]. The constants comply with the Born stability conditions, which require that C_{11} exceeds 0, C_{44} exceeds 0, $C_{11} - C_{12}$ exceeds 0 and $C_{11} + 2C_{12}$ exceeds 0. This confirms that both materials are mechanically stable at the imposed pressure [53].

The Cauchy pressure (C_p) is an essential mechanical parameter that significantly influences the comprehension of the ductile/brittle characteristics of a material. The mathematical representation is:

$$C_p = C_{12} - C_{44} \tag{3}$$

Both Sr_3BF_3 (B = As, Sb) photovoltaic compounds initially have a brittle nature, as evidenced by their negative Cauchy pressure (C_p). As pressure rises, there occurs a shift from a brittle to a ductile condition [20], resulting in greater positive values that indicate improved ductility.

The crystal stiffness (C_s) of a material quantifies its ability to resist the effect of shear stress when exerted on both in the [1 1 0] direction and the [1 1 0] plane, denoting its resilience against deformation caused by shear stress. The formula is defined as:

$$C_s = \frac{C_{11} - C_{12}}{2} \tag{4}$$

Table 4 presents the increase in crystal stiffness (C_s) in Sr_3BF_3 (B = As, Sb) materials when pressure is applied. This information emphasizes that the materials' capability to withstand plastic deformation is increased when pressure is exerted.

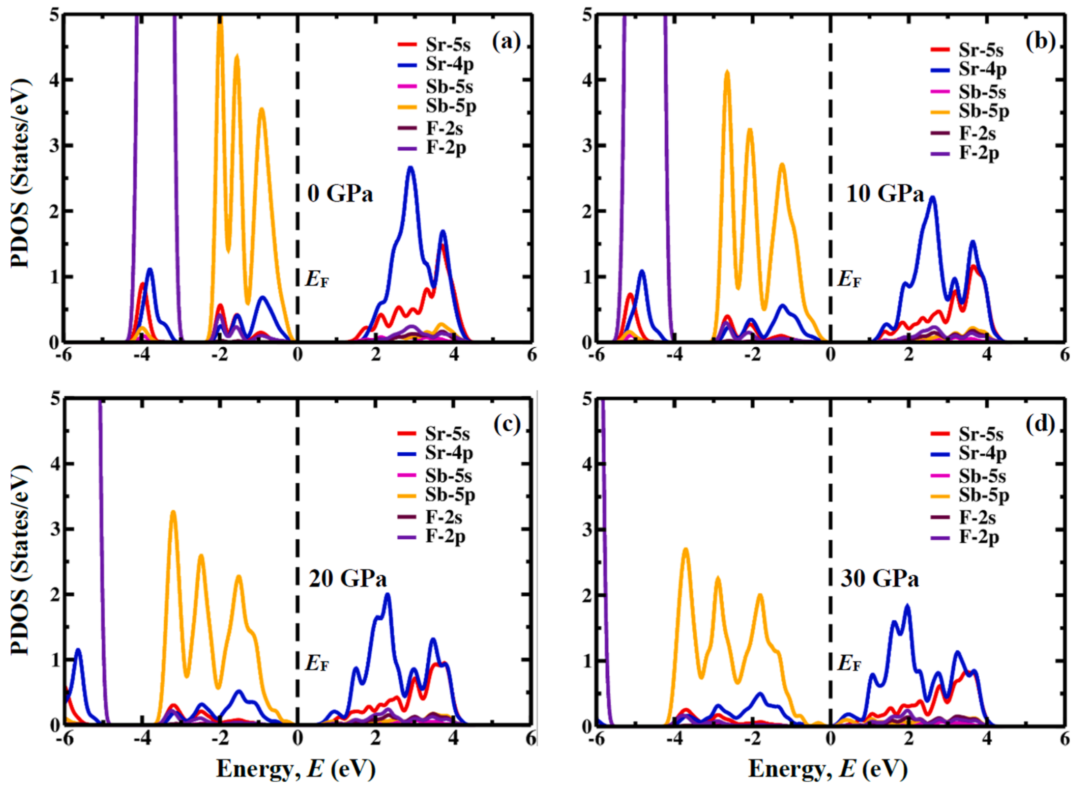

Fig. 12. Calculated partial density of states (PDOS) of Sr_3SbF_3 under different applied pressures.

Table 4
Calculated values of elastic constants C_{ij} (GPa), Crystal stiffness C_s (GPa), Cauchy pressure C_p (GPa), and Kleinman parameter ζ of Sr_3BF_3 (B = As, Sb) compounds under various applied pressures.

Pressure (GPa)	Compound	C_{11}	C_{12}	C_{44}	C_p	C_s	ζ
0	Sr_3AsF_3	82.71	12.03	19.70	−7.67	35.34	0.297
	Sr_3AsF_3 [22]	81.81	12.24	19.05	–	–	–
	Sr_3AsF_3 [23]	86.05	15.08	19.83	–	–	–
	Sr_3SbF_3	69.71	10.20	15.05	−4.84	29.75	0.298
10	Sr_3AsF_3	175.63	22.54	17.19	5.35	76.55	0.279
	Sr_3SbF_3	158.91	19.51	12.42	7.09	69.70	0.274
20	Sr_3AsF_3	255.95	31.50	12.78	18.73	112.22	0.274
	Sr_3SbF_3	235.71	27.27	7.93	19.34	104.22	0.266
30	Sr_3AsF_3	325.01	38.38	6.88	31.50	143.31	0.269
	Sr_3SbF_3	302.22	35.06	2.04	33.02	133.58	0.267

The Kleinman parameter, represented by the Greek character ζ and is dimensionless, typically ranges from zero to one. This parameter evaluates the degree to which bonds can be stretched relative to other forms of deformation. It measures the capability of the material to endure tensile forces and compressive forces. To compute the Kleinman parameter (ζ) for a given compound, we utilize the following formula:

$$\zeta = \frac{C_{11} + 8C_{12}}{7C_{11} + 2C_{12}} \tag{5}$$

As ζ approaches zero, the amount of bond bending is minimized,

Table 5
Calculated values of shear modulus G (GPa), bulk modulus B (GPa), Young's modulus Y (GPa), Pugh's ratio (B/G_H), hardness factor (H), machinability index (μ_M), and Poisson ratio (ν) of Sr_3BF_3 (B = As, Sb) under various applied pressures.

Pressure (GPa)	Compound	B	Y	G	μ_M	H	B/G_H	ν	A
0	Sr_3AsF_3	35.59	60.67	24.95	1.81	5.67	1.427	0.216	0.56
	Sr_3AsF_3 [22]	35.44	28.22	9.49	–	–	–	–	0.56
	Sr_3AsF_3 [23]	38.74	61.90	25.09	–	–	1.544	0.234	0.418
	Sr_3SbF_3	30.04	48.78	19.84	2.00	4.07	1.514	0.229	0.51
10	Sr_3AsF_3	73.57	85.96	32.93	4.28	3.03	2.234	0.305	0.22
	Sr_3SbF_3	65.98	71.08	26.91	5.31	1.81	2.451	0.320	0.18
20	Sr_3AsF_3	106.32	97.47	36.18	8.32	1.62	2.939	0.347	0.11
	Sr_3SbF_3	96.75	80.36	29.51	12.20	0.61	3.279	0.362	0.08
30	Sr_3AsF_3	133.92	99.84	36.29	19.46	0.55	3.691	0.376	0.05
	Sr_3SbF_3	124.11	80.74	29.01	60.81	−0.38	4.278	0.392	0.02

whereas when ζ approaches one, the amount of bond stretching is minimized. Table 4 illustrates the impact of pressure regarding the Kleinman parameter, specifically up to 30 GPa. The calculated ζ value suggests this material demonstrates characteristics of flexural bonding.

By using the elastic constants, we computed a number of mechanical variables of Sr_3BF_3 (B = As, Sb), including the bulk modulus (*B*), shear modulus (*G*), Young's modulus (*Y*), Poisson's ratio (*v*), Pugh's ratio (*B/G*) and Zener anisotropy index (*A*) as listed in Table 5. The Voigt-Reuss method is utilized to determine bulk and shear moduli (*B* and *G*), which establishes maximum and minimum values for the effective modulus in cubic lattices [54,55]. Hill's approach [56] posits that *B* and *G* represent the Voigt and Reuss values' arithmetic means, respectively. Additionally, the Poisson's ratio (*v*) and Young's modulus (*Y*) values can be determined using established equations. The data from previous studies for mechanical properties at 0 GPa pressure are agreeable with our study for Sr_3AsF_3 compound. Our findings for *B, Y, G, B/G, v,* and *A* for Sr_3AsF_3 are 35.59, 60.67, 24.95, 1.427, 0.216, 0.56 respectively. In comparison, for simulation under 0 GPa pressure in previous studies by Ali Algahtani et al. [22] shows values of *B, Y, G,* and *A* for Sr_3AsF_3 of 35.44, 28.22, 9.49, 0.56 respectively and Ghosh et al. [23] shows *B, Y, G, B/G, v,* and *A* for Sr_3AsF_3 of 38.74, 61.90, 25.09, 1.544, 0.234, 0.418 respectively which are comparable to our results. A material's bulk modulus (*B*) indicates its capacity to withstand fracturing, conversely, the shear modulus (*G*) represents its ability to resist plastic deformation. When the values of both *B* and *G* are raised, Sr_3AsF_3 exhibits greater fracture resistance and resistance to plastic deformation in comparison to Sr_3SbF_3. The comparison of Young's modulus (*Y*), a stiffness measure, indicates that Sr_3AsF_3 exhibits more stiffness than Sr_3SbF_3. Applying pressure enhances the resistance of the material to fracture and plastic deformation, while also enhancing its stiffness.

The machinability index is an important metric that indicates the efficiency of a machine for potential engineering applications. A greater value of μ_M indicates better lubrication, decreased friction during feeding, and increased plastic strain of the material. The hardness factor (*H*) determines how resistant a material is to deformation. The values of these parameters are determined by applying the formula provided below [55]:

$$\mu_M = \frac{B}{C_{44}} \tag{6}$$

$$H_v = 2\left(K^2G\right)^{0.585} - 3; \quad K = G/B \tag{7}$$

Table 5 reveals the relationship between pressure, machinability index, and hardness. The machinability index increases proportionally with the pressure. Sr_3BF_3 (B = As, Sb) photovoltaic compounds exhibit enhanced malleability under high-pressure conditions. Moreover, improved machinability allows for the use of more sophisticated and precise machining techniques, hence enabling the production of intricate device structures with higher performance and reliability. The hardness values of both compounds drop as pressure is increased. A reduction in the hardness factor shows an increase in the machinability index of Sr_3BF_3 (B = As, Sb). The material's lower hardness and greater Machinability index facilitate its malleability, allowing for easy bending, curving, and shaping into precise forms. Consequently, the production of various electronic and optoelectronic devices is comparatively effortless.

The value of Poisson's ratio (v) at 0.26 [57] is a crucial parameter for differentiating between ductile and brittle materials. Material possessing Poisson's ratio that exceeds 0.26 is categorized as ductile material. Thus, both Sr_3AsF_3 and Sr_3SbF_3 exhibit ductility under certain pressures but are otherwise brittle (Table 5). Pugh's ratio (*B/G*) is an additional indicator of ductility, with 1.75 as the critical threshold [58]. Our calculated *B/G* values suggest that both compounds become slightly ductile under pressure. Fig. 13 shows the brittle to ductile transition curve upon application of hydrostatic pressure. However, the ductility of Sr_3SbF_3 slightly exceeds that of Sr_3AsF_3. Notably, the trends in *v* and *B/G* [58–60] closely resemble the data of crystal stiffness (C_s) that quantifies the capacity of a material to endure shear stress as presented in Tables 4 and 5. Both *v* and *B/G* increase with pressure, indicating greater ductility.

Having a thorough comprehension of the significance of elastic anisotropy is essential in the domain of applied engineering. The measurement of directional dependence of characteristics is called anisotropy, which is quantified using the anisotropic index [61]. *A* is equal to 1 representing the isotropic nature of single crystals while any other value implies the anisotropy nature of crystals [62]. The Zener anisotropy factor is expressed as:

$$A = \frac{2C_{44}}{C_{11} - C_{12}} \tag{8}$$

The calculated anisotropic factors for Sr_3BF_3 (B = As, Sb) deviate from unity justifying their anisotropic nature. To further examine the anisotropic feature, The ELATE tool [33] was employed for modeling the changes in the Poisson ratio, shear modulus, and Young's modulus, as depicted in Fig. 14. The three-dimensional spherical graph demonstrates the existence of isotropic behavior, but material anisotropy is shown by the deviation from a spherical shape. The graph clearly demonstrates that the deviation from spherical patterns becomes more prominent with pressure. This suggests that applying pressure may enhance the anisotropy in Sr_3BF_3 (B = As, Sb).

The Debye temperature (θ_D) is essential for comprehending material phenomena, such as specific heat capacity and thermal expansion. Additionally, it provides valuable information regarding the alterations in a material's characteristics when exposed to different temperatures and pressures. Table 6 shows the Debye temperature's variation with temperature and pressure, calculated using the following formula [63,64]:

$$\Theta_D = \frac{h}{k_B}\left[\frac{3n}{4\pi}\left(\frac{N_A\rho}{M}\right)\right]^{\frac{1}{3}} v_m \tag{9}$$

The variables in the given equation consist of Planck's constant (*h*), Avogadro's number (N_A), Boltzmann's constant (k_B), density (ρ), molecular mass (*M*), and the velocity of sound (v_m). The Navier equation is used to determine the sound speed [64].

Table 6
Determined values of density ρ ($g\ cm^{-3}$), transverse sound velocity v_t ($m\ s^{-1}$), longitudinal sound velocity v_l ($m\ s^{-1}$), mean sound velocity v_m ($m\ s^{-1}$), Debye temperature $\theta_D(K)$ and melting temperature $T_m(K)$ of Sr_3BF_3 (B = As, Sb) from 0 to 30 GPa pressure.

Pressure (GPa)	Compound	ρ	v_t	v_l	v_m	θ_D	T_m
0	Sr_3AsF_3	3.53	2658.86	4417.13	2940.41	293.63	1041.83
	Sr_3SbF_3	3.44	2401.06	4051.48	2659.30	253.68	964.96
10	Sr_3AsF_3	4.16	2813.53	5314.37	3144.76	331.72	1590.99
	Sr_3SbF_3	4.17	2542.00	4945.24	2846.82	289.41	1492.14
20	Sr_3AsF_3	4.65	2790.67	5768.17	3136.40	343.25	2065.68
	Sr_3SbF_3	4.71	2502.74	5374.68	2818.27	298.52	1946.04
30	Sr_3AsF_3	5.05	2681.13	6009.67	3025.01	340.35	2473.80
	Sr_3SbF_3	5.16	2371.07	5616.69	2680.99	292.73	2339.11

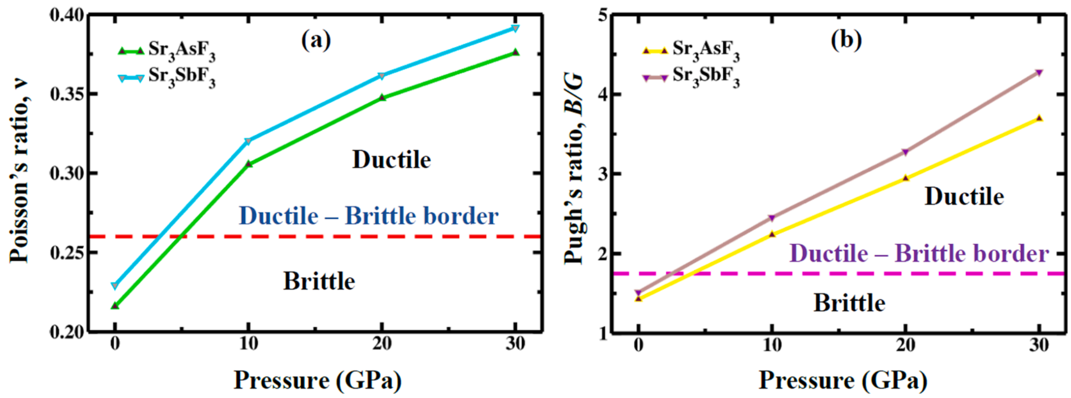

Fig. 13. (a) Poisson's ratio (ν) and (b) Pugh's ratio (B/G) of Sr_3BF_3 (B = As, Sb) with respect to applied pressures.

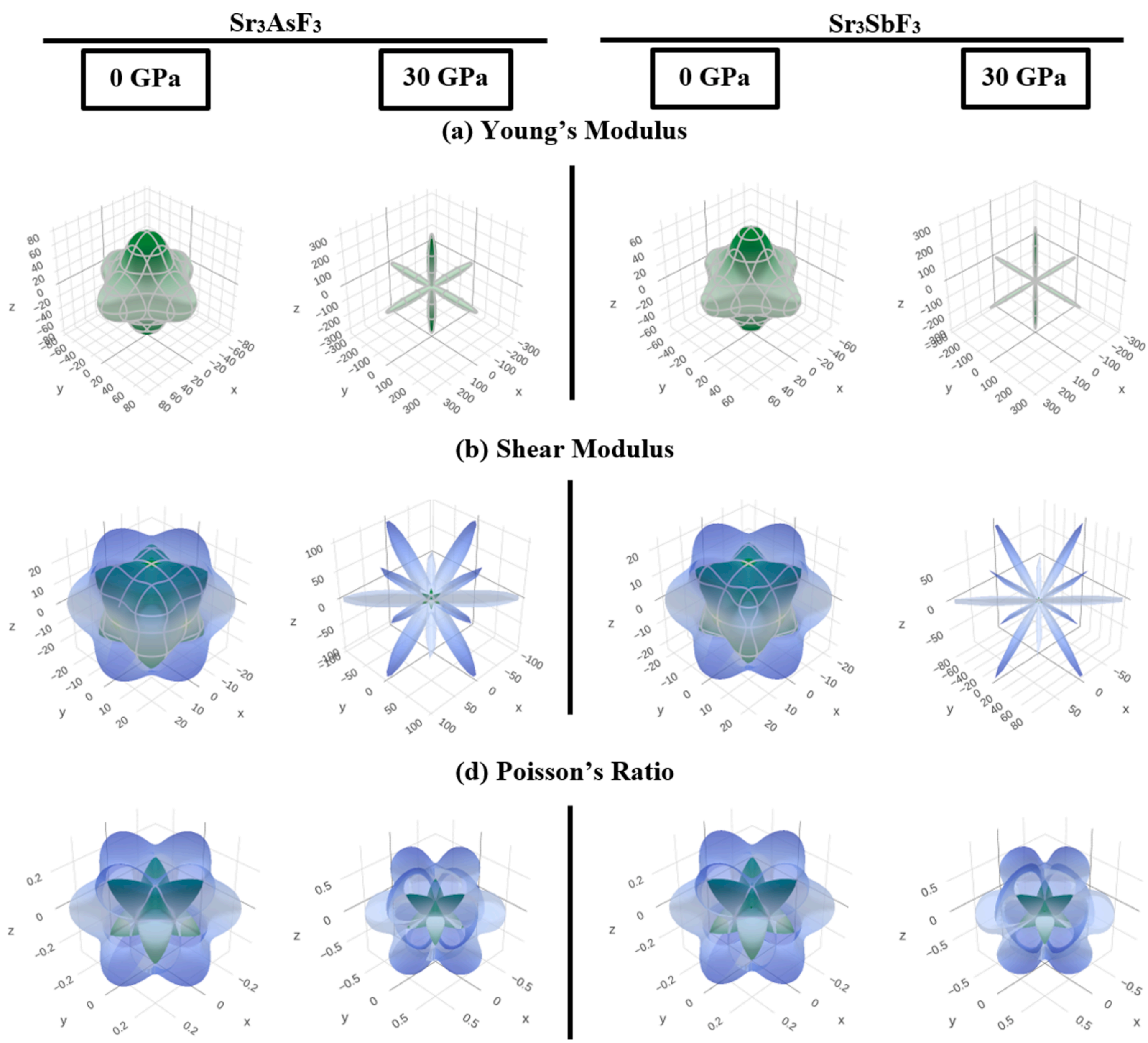

Fig. 14. 3D illustrations of (a) Young's Modulus, (b) Shear modulus, and (c) Poisson's ratio of Sr_3BF_3 (B = As, Sb) at 0 and 30 GPa.

$$v_m = \left[\frac{1}{3}\left(\frac{2}{v_s{}^3} + \frac{1}{v_l{}^3}\right)\right]^{-1/3} \tag{10}$$

To compute the sound velocity's longitudinal and transverse components, we can use the following formulas:

$$v_t = \sqrt{\frac{G}{\rho}} \tag{11}$$

$$v_l = \sqrt{\frac{3B+4G}{3\rho}} \tag{12}$$

The Debye temperatures (Θ_D) of Sr_3AsF_3 and Sr_3SbF_3 photovoltaic compounds were studied under different pressures. The findings show that the Debye temperature rises with pressure for both materials. For Sr_3AsF_3, Θ_D increases from 293.63 K under 0 GPa to 343.25 K under 20 GPa, while for Sr_3SbF_3, it increases from 253.68 K at 0 GPa to 298.52 K at 20 GPa. This rise indicates that the lattice stiffness of these materials improves with pressure up to 20 GPa, enhancing their vibrational properties and potentially improving their performance in mechanical applications under high pressure. However, at 30 GPa, the Θ_D values for both materials decrease, suggesting that further pressure increases may reduce performance.

Another important parameter that we can obtain using elastic constants is the melting temperature (T_m) which is expressed as [65]:

$$T_m = (554 + 5.911C_{11}) \tag{13}$$

The melting temperatures (T_m) of Sr_3AsF_3 and Sr_3SbF_3 photovoltaic compounds were investigated under various pressures, as shown in Table 6. The data reveals that the melting temperature increases with pressure for both compounds. For Sr_3AsF_3, T_m ranges from 1041.83 K under 0 GPa to 2473.80 K under 30 GPa, while for Sr_3SbF_3, T_m ranges from 964.96 K under 0 GPa to 2339.11 K under 30 GPa. This pattern indicates that both materials demonstrate improved thermal stability under higher pressures, which is crucial for their potential applications in high-temperature environments.

3.5. Optical properties

A thorough investigation of the optical characteristics of Sr_3AsF_3 and Sr_3SbF_3 photovoltaic compounds is crucial to determine their viability for usage in solar applications. The analysis involves the examination of several parameters, such as the absorption coefficient $\alpha(\omega)$, conductivity $\sigma(\omega)$, refractive index $n(\omega)$, complex dielectric function $\varepsilon(\omega)$, extinction coefficient $k(\omega)$, reflectivity $R(\omega)$ and loss function $L(\omega)$. Complex dielectric constant $\varepsilon(\omega)$ comprises two components: The real part is represented by $\varepsilon_1(\omega)$, and the imaginary part is indicated by $\varepsilon_2(\omega)$. The definition of the dielectric function is expressed as,

$$\varepsilon(\omega) = \varepsilon_1(\omega) + j\varepsilon_2(\omega) \tag{14}$$

The real component, $\varepsilon_1(\omega)$, symbolizes the response of the material to light transmission, while the amount of light absorbed is represented by the imaginary component $\varepsilon_2(\omega)$. The initial static value of the dielectric constant, $\varepsilon_1(0)$, is 3.60 found for Sr_3AsF_3 and 3.62 for Sr_3SbF_3 at 0 GPa. These values grow to 8.7 and 10.6 at 30 GPa, respectively, as depicted in Fig. 15(a). The first maximum energy levels detected for Sr_3AsF_3 and Sr_3SbF_3 are 2 eV, along with 0.50 eV and 0.35 eV at a pressure of 30 GPa, respectively. Bandgap energy and the static dielectric constant $\varepsilon_1(0)$ calculated values are consistent with Penn's model [66]. A negative dielectric function (ε_1) was observed within the range of energy of 8.30–8.50 eV for Sr_3AsF_3, 7.40–7.90 eV for Sr_3SbF_3 at 0 GPa which shifts towards 12.30–12.50 eV for Sr_3AsF_3 and 10.80–11.30 eV for Sr_3SbF_3 at 30 GPa, According to Fig. 15(b), $\varepsilon_2(\omega)$ is associated with the inter-band transition that occurs when light energy is absorbed, and it is directly related to the band structure [67]. Significantly, at 30 GPa pressure Sr_3AsF_3 and Sr_3SbF_3 show notable peaks in the area that is visible. Sr_3SbF_3 is prioritized due to its small band gap, which facilitates transitions with lower-energy photons.

In order to ascertain the optical characteristics of Sr_3BF_3, in this study we may compute its optical absorption coefficient $\alpha(\omega)$ along with

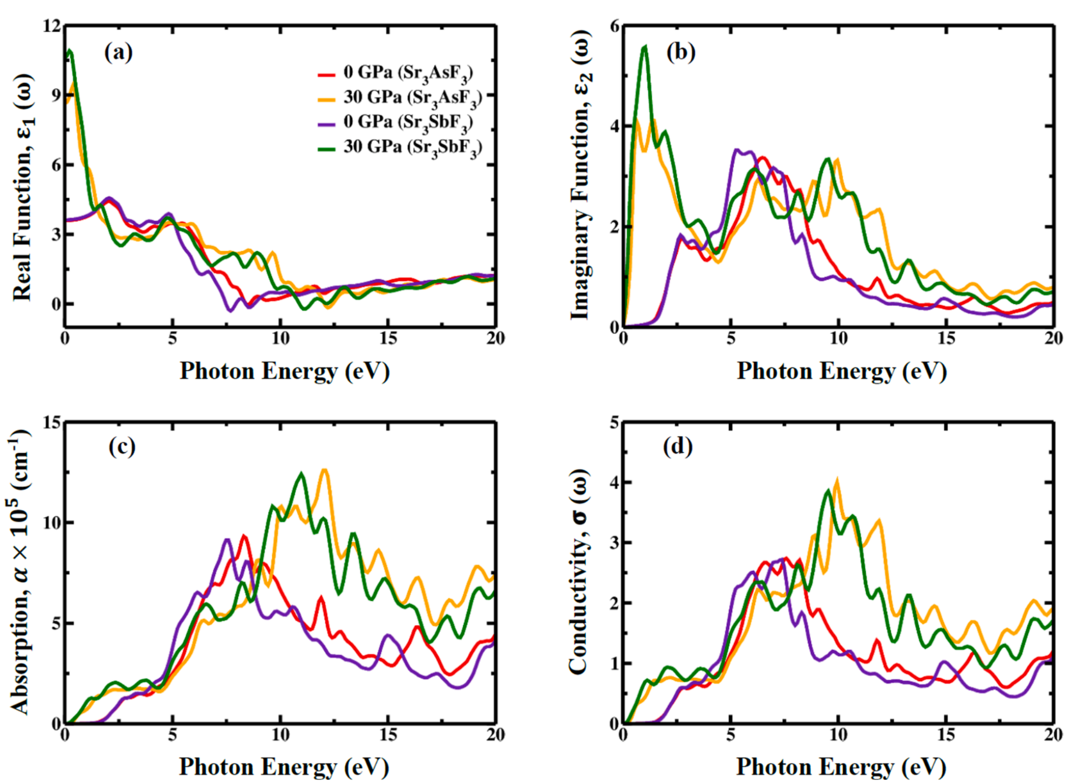

Fig. 15. Impact of pressure on (a) real function, (b) imaginary function, (c) absorption, and (d) optical conductivity of Sr_3BF_3 (B = As, Sb) materials.

its optical conductivity $\sigma(\omega)$ using the following formulas [68]:

$$\alpha(\omega) = \frac{\sqrt{2}\omega\left[\{\varepsilon_1^2(\omega)+\varepsilon_2^2(\omega)\}^{\frac{1}{2}}-\varepsilon_1(\omega)\right]^{\frac{1}{2}}}{c} \tag{15}$$

$$\sigma(\omega) = \frac{\alpha(\omega)n(\omega)c}{4\pi} \tag{16}$$

One useful parameter for determining a material's nature is the optical absorption coefficient, such as in case it exhibits characteristics that are metallic, semiconducting or insulating. This coefficient also aids in determining the optimal solar energy conversion efficiency (OSECE). Under zero pressure, in both compounds, the spectra of optical absorption come from their respective band gap energy, as illustrated in Fig. 15(c), demonstrating their semiconducting nature. However, a transition towards lower photon energy (redshift) is observed under high pressure for both systems, as evidenced by the EBS calculations. Additionally, a high absorption spectrum is found across a broad electromagnetic range (6.80–15.00 eV) within the spectrum of ultraviolet light, reaching its peak under high pressure.

One further essential aspect of optical properties is optical conductivity $\sigma(\omega)$, which estimates a material's ability to conduct electricity when illuminated by light [69]. This characteristic is contingent upon the mobility and concentration of unbound charge carriers. Fig. 15(d) displays spectra with a noticeable peak with low photon energies and sharp peaks at high energies. Furthermore, the impact of pressure is observable, since the maximum heights of the $\sigma(\omega)$ spectra escalate with increasing pressure for both substances. Both materials show modest peaks under extreme pressure, in the low-energy photon range, as illustrated in Fig. 15(d). This suggests that these materials have the possibility of utilization in optoelectronic devices and solar panels that function in the range of low-energy photons. Moreover, the following formulas [68] were used to calculate the refractive index $n(\omega)$, extinction coefficient $k(\omega)$, reflectivity $R(\omega)$, and energy loss function $L(\omega)$:

$$n(\omega) = \frac{\left[\left(\varepsilon_1^2(\omega)+\varepsilon_2^2(\omega)\right)^{\frac{1}{2}}+\varepsilon_1(\omega)\right]^{\frac{1}{2}}}{\sqrt{2}} \tag{17}$$

$$k(\omega) = \frac{\left[\left(\varepsilon_1^2(\omega)+\varepsilon_2^2(\omega)\right)^{\frac{1}{2}}-\varepsilon_1(\omega)\right]^{\frac{1}{2}}}{\sqrt{2}} \tag{18}$$

$$R(\omega) = \frac{[n(\omega)-1]^2+k(\omega)^2}{[n(\omega)+1]^2+k(\omega)^2} \tag{19}$$

$$L(\omega) = \frac{\varepsilon_2(\omega)}{\varepsilon_1^2(\omega)+\varepsilon_2^2(\omega)} \tag{20}$$

The amounts of electromagnetic waves that are reflected and blocked from flowing through the material are represented by the refractive index $n(\omega)$, as depicted in Fig. 16(a). Finding the right optical material for use in a wide range of optoelectronic devices like optical waveguides, solar panels, light emitting diodes (LEDs), and detectors, requires a thorough understanding of the real component of the refractive index n (x) [20,70]. According to Fig. 16(a), the static refractive index values at zero frequency, or $n(0)$, are approximately 1.90 for both compounds at 0 GPa and rise to approximately 2.94 and 3.25 at 30 GPa for Sr_3AsF_3 and Sr_3SbF_3, respectively. A significant amount of the illuminated light can be absorbed by both systems because their static refractive indices [n (0)] are high at 30 GPa (Fig. 16a). Most notably, compared to certain possible cubic compounds for optoelectronic and solar device applications, very high values of $n(\omega)$ are observed at zero photon energy [71]. Particularly, values of $n(\omega)$ and peak maximum position are shown to be closely related in comparison to $\varepsilon_1(\omega)$. The relationship between real part of the dielectric function $\varepsilon_1(\omega)$ and refractive indices $n(\omega)$, which can be expressed in the formula: $n^2(\omega) - k^2(\omega) = \varepsilon_1(\omega)$, is highlighted by this correlation.

An object's extinction coefficient or $k(\omega)$ is a measure of how much light it can absorb. It is similar to ε_2 (ω) and may be seen in Fig. 16(b).

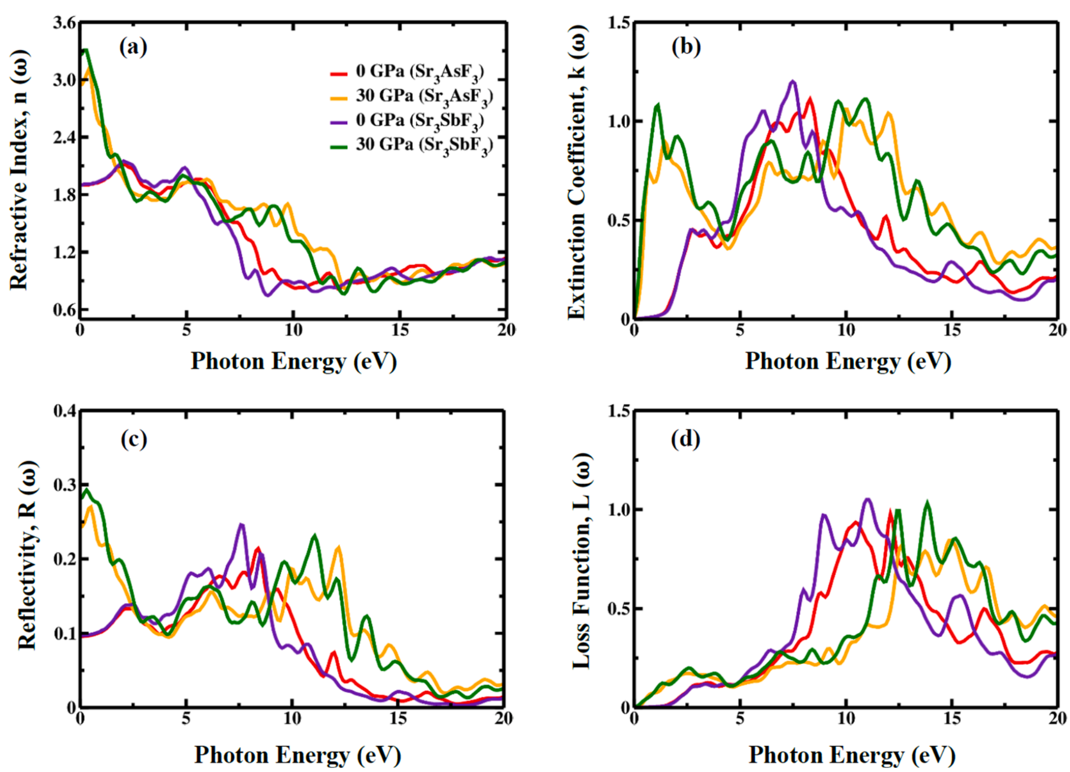

Fig. 16. Influences of applied pressure on (a) refractive index, (b) extinction coefficient, (c) reflectivity, and (d) loss function of Sr_3BF_3 (B = As, Sb) materials.

Eq. (21) [72] expresses the Kramer-Kronig relationship, which establishes this relationship between $k(\omega)$ and $\varepsilon_2(\omega)$.

$$\varepsilon_2(\omega) = \frac{e^2 h}{\pi m^2 \omega^2} \sum_{v,c} \int |M_{ev}(k)|^2 \delta[\omega_{ev}(k) - \omega] d^3k \tag{21}$$

The reflectivity $R(\omega)$ of Sr_3BF_3, as shown in Fig. 16(c), gives a formal picture of how much electromagnetic radiation a material reflects when light hits its surface. The constant values of $R(0)$ that we have obtained are 10 %, 10 %, 24.5 %, and 28 % for Sr_3AsF_3 (under 0 GPa), Sr_3SbF_3 (under 0 GPa), Sr_3AsF_3 (under 30 GPa), and Sr_3SbF_3 (under 30 GPa). The scientific community is well aware of the relationship between a material's low reflectivity and strong light absorption/transmission. As can be observed from Fig. 16(c), the $R(\omega)$ displays relatively low values (>44 %) in the IR-visible (low energy) area [19,20]. Moreover, throughout the whole photon energy range, the $R(\omega)$ spectra of the two photovoltaic compounds under study exhibit a slightly higher peak at high pressure. It is possible to deduce a low $R(\omega)$ from critical value (44 %), which indicates that the incident light has a strong absorptivity/transitivity, The optimum photon absorption capacity of these compounds makes them good candidates for utilization in optoelectronic devices.

Fig. 16(d) shows the energy loss function $L(\omega)$. The amount of energy reflected or scattered by the material can be due to different factors. Under pressured conditions, the value of $L(\omega)$ within the visible and ultraviolet energy ranges is less than 0.20 and 1.05, respectively, indicating minor emissions within these wavelength ranges. Using a low value for this in a material facilitates faster movement of holes and electrons through it. Lastly, due to their important qualities, the materials under high pressure that have been investigated may spark a great deal of curiosity among researchers.

3.6. Thermodynamic properties

To verify the thermodynamic stability of Sr_3AsF_3 and Sr_3SbF_3, the thermal properties were examined using the Gibbs2 algorithm [36], which is based on the Debye model's quasi-harmonic approximation [73]. Similar to this, we have studied thermal properties such as entropy (S), thermal expansion (α), specific heat (C_V) and Grüneisen parameter (γ), which are plotted against temperature as shown in Figs. 17 and 18.

The specific heat (C_V), which measures the temperature change of a material in response to energy input, establishes a causal relationship between the material's dynamics. The specific heat profiles for Sr_3AsF_3 and Sr_3SbF_3 are demonstrated in Figs. 17(a) and 18(a) respectively. With temperature, the specific heat (C_V) rises and becomes closer to the Dulong–Petit limit. The figures make it abundantly evident that at decreasing pressures, the value of (C_V) increases. This suggests that, as the temperature rises, the material's heat capacity increases until it reaches a point where it stabilizes according to the Dulong–Petit law [74]. This value for Sr_3AsF_3 and Sr_3SbF_3 are same at 172 J/molK. Further evidence that pressure significantly affects a material's thermal properties comes from the statistics, which show that the material exhibits a greater specific heat at lower pressures. As the pressure increases, the system is compressed, which increases the system's internal energy. Higher pressures cause a decrease in the specific heat (C_V) [75].

To explain the anharmonic effects seen in a material when it undergoes variations in pressure and volume, Eduard Gruneisen proposed the idea of "thermal pressure," which defines how pressure rises with heat and temperature. Figs. 17(b) and 18(b) show the variation of the Grüneisen parameter (γ) for Sr_3AsF_3 and Sr_3SbF_3, respectively. These graph shows the value of γ slightly increases with temperature for material under low pressure but for material under high hydrostatic pressure, this value slightly decreases with temperature. Increased pressure also results in an overall greater value of γ which can be attributed to phase transition due to pressure.

A material's configuration, including its length, area, and volume, changes as its temperature rises. In thermophysical nomenclature, the symbol "α" stands for this phenomenon, which is also referred to as thermal expansion. Figs. 17(c) and 18(c) show the thermal expansion alternation Sr_3AsF_3 and Sr_3SbF_3, respectively. The graphs show that as the temperature rises, the coefficient of thermal expansion, or α, finally approaches a constant value. Furthermore, as pressure rises, α falls. This

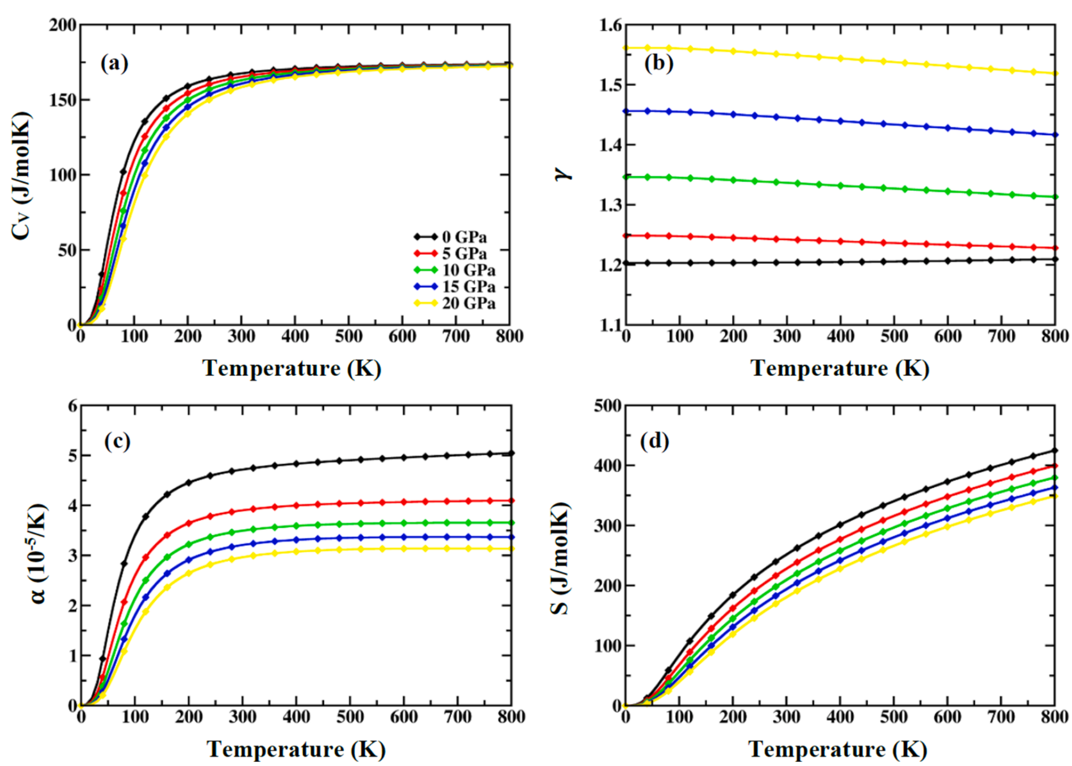

Fig. 17. Changes of (a) Specific heat, (b) Grüneisen parameter, (c) Thermal expansion, and (d) Entropy of Sr_3AsF_3 as a function of temperature.

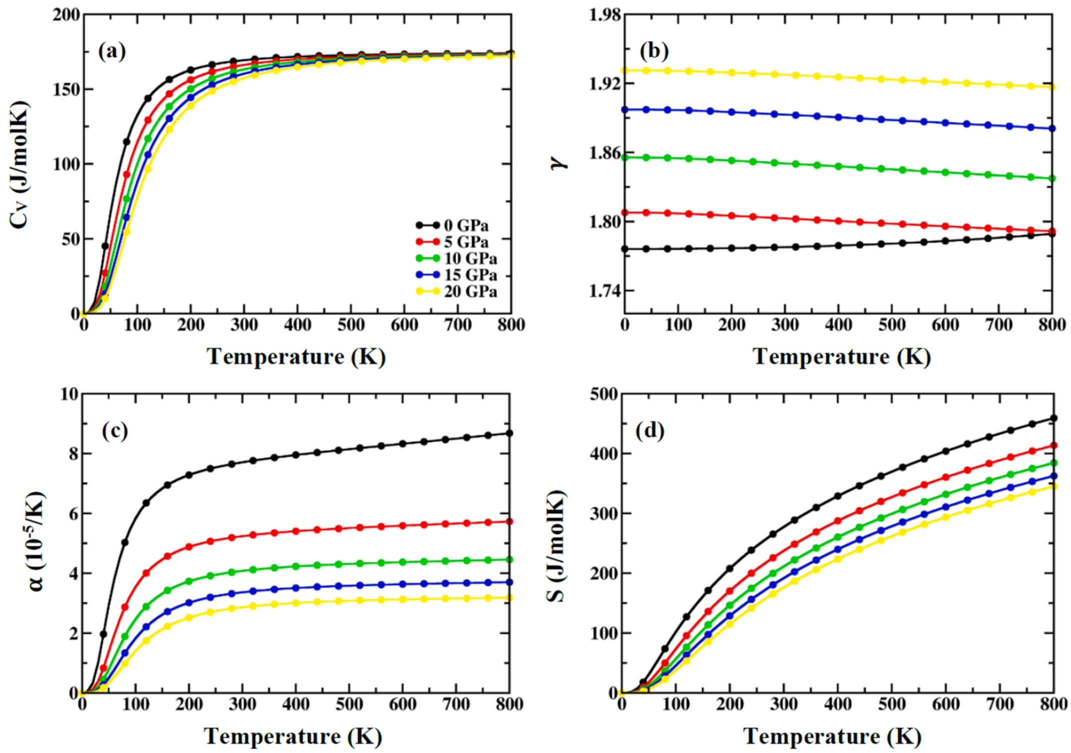

Fig. 18. Changes of (a) Specific heat, (b) Grüneisen parameter, (c) Thermal expansion, and (d) Entropy of Sr_3SbF_3 as a function of temperature.

happens because atoms and molecules move harmonically when they are at their positions of equilibrium. They acquire more kinetic energy as the temperature rises, leading to increased vibrations and movements. This results in greater interatomic distances and thus, material expansion. On the other hand, applying pressure limits the lengthening of the bonds, which lessens the material's expansion.

Entropy (S) quantifies the level of chaos and unpredictability in a system, making it a dependable tool for forecasting the system's physical

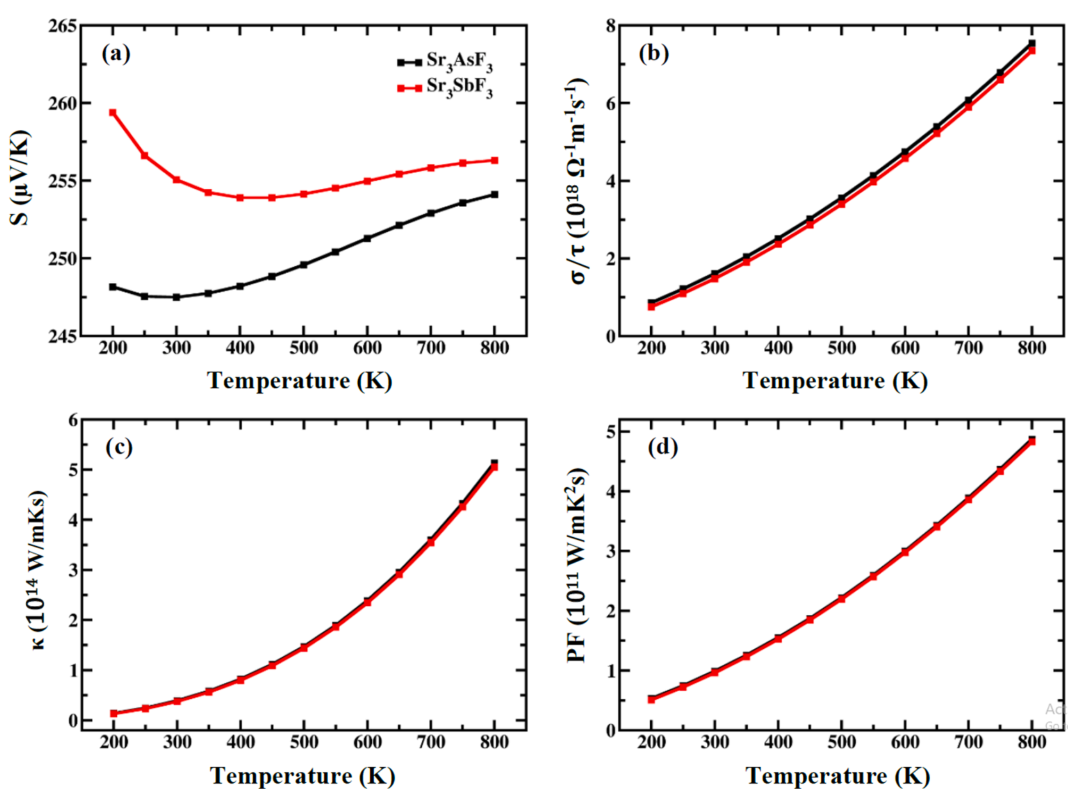

Fig. 19. Changes of (a) Seebeck coefficient, (b) Electrical conductivity, (c) Total Thermal conductivity, and (d) Power factor of Sr_3BF_3 (B = As, Sb) as a function of temperature.

condition. As shown in Figs. 17(d) and 18(d) for Sr_3AsF_3 and Sr_3AsF_3 respectively, the entropy value starts at zero for all pressure at 0 K temperature. Entropy (*S*) rises exponentially with temperature but diminishes as pressure increases. Increased pressure results in a decline in volume, causing the system's components to become more concentrated in a smaller area, leading to a reduction in entropy. The entropy of Sr_3AsF_3 is determined to be 424.85 J mol^{-1} K^{-1} at 800 K temperature and 0 GPa pressure. Additionally, the entropy of Sr_3AsF_3 is found to be 459.26 J mol^{-1} K^{-1}. The increase in entropy is a result of the heightened vibrational movement of atoms due to the temperature increase, causing the system's internal energy to increase. Notably, the entropy curve maintains a seamless and uninterrupted pattern, suggesting that the material stays in the same phase over the whole temperature range.

3.7. Thermoelectric properties

The thermoelectric coefficients are used for finding the potential of wasted heat energy recovery of a material. The BoltzTraP [37] is a software package designed for the computation of thermoelectric properties, such as the Seebeck coefficient (*S*), electrical conductivity (σ), Total Thermal conductivity (κ), Power factor (*PF*) and figure of merit (*ZT*). These coefficients are illustrated in a range of 0 K up to 800 K temperature in Figs. 19**(a–d) and** 20 accordingly. The dimensionless figure of merit (*ZT*) is the main figure used to evaluate the effectiveness of thermoelectric materials, which is given in a condensed format:

$$ZT = S^2\sigma T/\kappa \tag{22}$$

The terms in the equation described above have precise definitions, as emphasized in fundamental investigations carried out in other significant research [76–78]. An examination of the thermoelectric properties provides valuable insights into the suitability of a material for commercial thermoelectric applications can be ascertained via the numerical value of (ZT). A material is considered a good thermoelectric material when its thermoelectric figure of merit (*ZT*) is equal to 1. We have investigated these compounds to assess their thermoelectric behavior across several temperature ranges and to identify their potential suitability for thermoelectric applications.

The Seebeck coefficient (*S*) describes what amount of thermoelectric voltage produced in response to a thermal gradient across it. A high Seebeck coefficient typically corresponds to a high figure of merit value which means a higher efficiency when thermal energy to electrical energy and vice-versa. As we can see in Fig. 19(a)**,** materials with narrower band gaps show a substantially better value of the Seebeck coefficient as Sr_3SbF_3 is more efficient than Sr_3AsF_3. The upper limit of the Seebeck coefficient for Sr_3SbF_3 is similarly found at 259 μV/K under 200 K temperature and for Sr_3AsF_3 this value is 254 μV/K under 800 K temperature. Additionally, we see the fact that both compounds behave differently while increasing temperature.

Electrical conductivity per relaxation time against these compounds is illustrated in Fig. 19(b)**,** which corresponds to the electron transport behavior with a temperature gradient. Both materials have a consistent behavior, as their conductivity demonstrates an approximately linear growth with increasing temperature. The maximum conductivity observed for Sr_3AsF_3 is 7.539 × 1018 $\Omega^{-1}m^{-1}s^{-1}$ at a temperature of 800 K, while for Sr_3SbF_3 it is 8.929 × 1018 $\Omega^{-1}m^{-1}s^{-1}$ at the same temperature. The increased conductivity at higher temperatures can be due to the favorable effect of thermal energy on the concentration of charge carriers, which in turn facilitates electron transfer between the valence band (VB) and the conduction band (CB).

Thermal conductivity (κ), consists of both electronic and lattice constituents. The electrical component is generated through the conduction of heat energy by electrons, whereas the lattice component is a result of the lattice structure's vibrations. The total thermal conductivity against temperature is depicted in Fig. 19(c)**,** which shows an increasing trend for both compounds. Both show similar values at similar temperatures with the lowest at 200 K with 0.14 × 10^{14} W/mKs for Sr_3AsF_3 and 0.13 × 10^{14} W/mKs for Sr_3SbF_3. The maximum value is similarly found at the highest temperature of 800 K with 5.13 × 10^{14} W/mKs for Sr_3AsF_3 and 6.86 × 10^{14} W/mKs for Sr_3SbF_3. Thermal conductivity, like electrical conductivity, is affected by the charge carrier concentration. Therefore, a rise in temperature causes an increment in the value of this parameter. Nevertheless, thermal conductivity exhibits a significant increase as temperature rises, in contrast to electrical conductivity. The findings are in good agreement with the Wiedemann-Franz law, which demonstrates their clear relationship, represented as [76]:

$$\kappa = \sigma LT \tag{23}$$

Fig. 19(d) displays the Power Factor (*PF*) curve with respect to temperature. The graph shows a nearly linear increase in this parameter as the temperature increases. The power factor is a parameter that takes into account both the Seebeck coefficient and electrical conductivity, which explains its behavior being similar to them. At 200 K temperature, Sr_3AsF_3 and Sr_3SbF_3 show *PF* values at 0.53 × 10^{11} W/mK^{2}s and 0.51 × 10^{11} W/mK^{2}s respectively. Similarly, at 800 K temperature, the highest value is found which are for Sr_3AsF_3 and Sr_3SbF_3, 4.87 × 10^{11} W/mK^{2}s and 5.86 × 10^{11} W/mK^{2}s respectively.

Fig. 20 illustrates the correlation between chemical potential and the thermoelectric figure of merit (*ZT*) at various temperatures for the listed compounds. The relationship shown by (*ZT*) demonstrates that reduces with increasing thermal conductivity while it increases with higher electrical conductivity and Seebeck coefficient. We can see the effect of a narrower band gap here which leads the value closer to unity as is the case with Sr_3SbF_3 which has a value for (*ZT*) of 0.78 at 200 K temperature but Sr_3AsF_3 has a value of 0.76 in a similar temperature range. The effect of increased temperature is not ideal as for both materials the value of *ZT* strays further from unity.

4. Conclusion

The DFT approach was employed in this study to explore the structural, electronic, mechanical, optical, thermodynamic, and thermoelectrical properties of the photovoltaic compounds Sr_3BF_3 (B = As, Sb). We have utilized TB-mBJ functional addition to GGA-PBE functional for more accurately calculating electronic parameters in ground state condition. Our study found that the band gaps of Sr_3AsF_3 and Sr_3SbF_3 drop from 3.26 and 2.95 eV to 1.36 and 0.99 eV respectively due to pressure. The compounds exhibit mechanical stability owing to the crystal's elastic constant meeting the Born stability criteria under pressure. Additionally, the compound's negative formational enthalpy provides

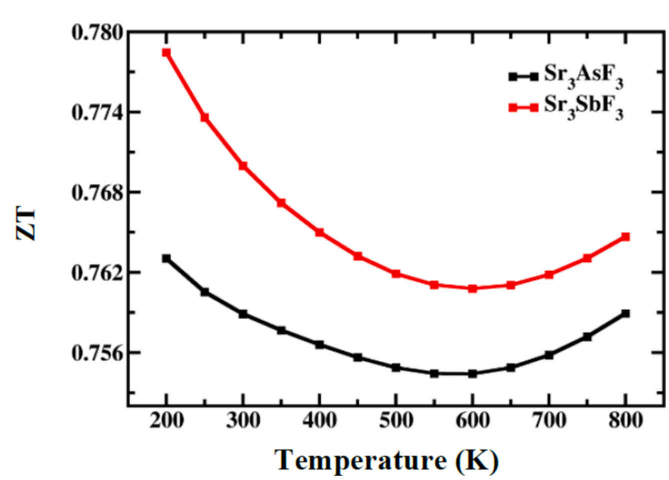

Fig. 20. Changes in figure of merit as a function temperature of Sr_3BF_3 (B = As, Sb).

chemical and thermodynamic stability and phonon stability was also verified. The mechanical properties, including elastic constants, bulk modulus, shear modulus, and Young's modulus, exhibit significant improvement under increased pressure. An analysis of Poisson's ratio, Pugh's ratio, and Cauchy pressure indicate that Sr_3BF_3 compounds possess a ductile characteristic in pressurized conditions and ductility further increases with pressure. Under hydrostatic pressure, Sr_3BF_3 photovoltaic compounds showed a noticeable red shift and increased absorption and optical conductivity peaks. This shows that pressure can improve the efficiency of Sr_3BF_3 photovoltaic compounds, which makes them optimal for application in solar cells and other kinds of optoelectronic devices. Thermodynamic properties evaluated at various temperatures satisfy Dulong–Petit law for varied pressured circumstances and are high-temperature stable. Thermal efficiency is generally improved by a narrower band gap and decreased by temperature. The thermoelectric qualities of the compounds suggest they could be used in thermoelectric devices.

CRediT authorship contribution statement

Muneef Hasan: Writing – review & editing, Writing – original draft, Methodology, Investigation, Formal analysis, Data curation, Conceptualization. **Adil Hossain:** Writing – review & editing, Writing – original draft, Methodology, Investigation, Formal analysis, Data curation, Conceptualization. **Heider A. Abdulhussein:** Writing – review & editing, Writing – original draft, Software, Methodology, Investigation. **Abdullah Al Shadi:** Writing – review & editing, Writing – original draft, Methodology. **Bijoy Sorker:** Writing – review & editing, Writing – original draft, Investigation. **Ahmed Adnan Al-Khafagi:** Writing – review & editing, Validation, Formal analysis. **Redi Kristian Pingak:** Writing – review & editing, Validation, Investigation. **Diana Dahliah:** Writing – review & editing, Software, Methodology, Investigation. **Mohammed S. Abu-Jafar:** Writing – review & editing, Validation, Methodology, Investigation. **Asif Hosen:** Writing – review & editing, Writing – original draft, Supervision, Software, Methodology, Investigation, Formal analysis, Data curation, Conceptualization.

Declaration of competing interest

The authors declare that they have no known competing financial interests or personal relationships that could have appeared to influence the work reported in this paper.

Data availability

Data will be made available on request.

References

[1] L.C. Andreani, A. Bozzola, P. Kowalczewski, M. Liscidini, L. Redorici, Silicon solar cells: toward the efficiency limits, Adv. Phys.: X 4 (2019) 1548305, https://doi.org/10.1080/23746149.2018.1548305.

[2] J.H. Werner, J. Mattheis, U. Rau, Efficiency limitations of polycrystalline thin film solar cells: case of Cu(In,Ga)Se2, Thin Solid Films 480–481 (2005) 399–409, https://doi.org/10.1016/j.tsf.2004.11.052.

[3] E.D. Kosten, J.H. Atwater, J. Parsons, A. Polman, H.A. Atwater, Highly efficient GaAs solar cells by limiting light emission angle, Light Sci. Appl. 2 (2013) e45–e, https://doi.org/10.1038/lsa.2013.1.

[4] J.P. Wilcoxon, G.A. Samara, P.N. Provencio, Optical and electronic properties of Si nanoclusters synthesized in inverse micelles, PhysRevB 60 (1999) 2704–2714, https://doi.org/10.1103/PhysRevB.60.2704.

[5] M. Husain, N. Rahman, A.H. Reshak, A. Habib, S. Ali, A. Laref, A.M. Al Bakri, J. Bila, Insight into the physical properties of the inter-metallic titanium-based binary compounds, Eur. Phys. J. plus 136 (2021) 624.

[6] N. Rahman, M. Husain, J. Yang, G. Murtaza, M. Sajjad, A. Habib, A. Karim, Zulfiqar, M.U. Haq, A. Rauf, First principle study of structural, electronic, elastic, and magnetic properties of half-Heusler compounds ScTiX (X= Si, Ge, Pb, In, Sb, and Tl), J. Supercond. Nov. Magn. 33 (2020) 3915–3922.

[7] X. Huang, D. Ji, H. Fuchs, W. Hu, T. Li, Recent progress in organic phototransistors: semiconductor materials, device structures and optoelectronic applications, ChemPhotoChem 4 (2020) 9–38, https://doi.org/10.1002/cptc.201900198.

[8] A. Kojima, K. Teshima, Y. Shirai, T. Miyasaka, Organometal halide perovskites as visible-light sensitizers for photovoltaic cells, J. Am. Chem. Soc. 131 (2009) 6050–6051, https://doi.org/10.1021/ja809598r.

[9] T.W. Kelley, P.F. Baude, C. Gerlach, D.E. Ender, D. Muyres, M.A. Haase, D.E. Vogel, S.D. Theiss, Recent progress in organic electronics: materials, devices, and processes, Chem. Mater. 16 (2004) 4413–4422, https://doi.org/10.1021/cm049614j.

[10] J. Chen, H. Dong, J. Li, X. Zhu, J. Xu, F. Pan, R. Xu, J. Xi, B. Jiao, X. Hou, K. Wei NG, S.-P. Wang, Z. Wu, Solar cell efficiency exceeding 25% through Rb-based perovskitoid scaffold stabilizing the buried perovskite surface, ACS Energy Lett. 7 (2022) 3685–3694, https://doi.org/10.1021/acsenergylett.2c01661.

[11] M.A. Green, A. Ho-Baillie, H.J. Snaith, The emergence of perovskite solar cells, Nat. Photonics 8 (2014) 506–514, https://doi.org/10.1038/nphoton.2014.134.

[12] H.S. Jung, N. Park, Perovskite solar cells: from materials to devices, Small 11 (2015) 10–25, https://doi.org/10.1002/smll.201402767.

[13] S.D. Stranks, G.E. Eperon, G. Grancini, C. Menelaou, M.J.P. Alcocer, T. Leijtens, L. M. Herz, A. Petrozza, H.J. Snaith, Electron-hole diffusion lengths exceeding 1 micrometer in an organometal trihalide perovskite absorber, Science 342 (2013) 341–344, https://doi.org/10.1126/science.1243982.

[14] M.F. Rahman, M.N.H. Toki, A. Irfan, A.R. Chaudhry, R. Rahaman, M. Rasheduzzaman, M.Z. Hasan, A novel investigation of pressure-induced semiconducting to metallic transition of lead free novel Ba 3 SbI 3 perovskite with exceptional optoelectronic properties, RSC Adv. 14 (2024) 11169–11184.

[15] M.A.U. Islam, O. Das, D.B. Khadka, M.R. Islam, M.F. Rahman, S. Kato, T. Soga, Effect of low to high pressure on the structural, mechanical, electrical, and optical properties of inorganic material Ca3AsBr3: an ab initio investigation, ACS Omega 9 (2024) 8005.

[16] A. Hosen, Investigating the effects of hydrostatic pressure on the physical properties of cubic Sr3BCl3 (B = As, Sb) for improved optoelectronic applications: A DFT study, Heliyon 10 (2024), https://doi.org/10.1016/j.heliyon.2024.e35855.

[17] A. Ghosh, M.F. Rahman, A. Kuddus, M.K. Mohammed, M.R. Islam, S. Bhattarai, A. R. Chaudhry, A. Irfan, Investigating of novel inorganic cubic perovskites of A3BX3 (A= Ca, Sr, BP, As, X= I, Br) and their photovoltaic performance with efficiency over 28%, J. Alloy. Compd. 986 (2024) 174097.

[18] M.A. Rahman, M.F. Rahman, L. Marasamy, Md. Harun-Or-Rashid, A. Ghosh, A. R. Chaudhry, A. Irfan, Impact of A-cations modified on the structural, electronic, optical, mechanical, and solar cell performance of inorganic novel A3NCl3 (A = Ba, Sr, and Ca) perovskites, Energy Fuels 38 (2024) 8199–8217, https://doi.org/10.1021/acs.energyfuels.4c00525.

[19] S. Joifullah, M.A. Hossain, M. Al Yeamin, M.M. Haque, R.K. Pingak, N.F. A. Mohammad, M.S. Abu-Jafar, A.A. Mousa, A. Hosen, First-principles investigation of pressure-modulated structural, electronic, mechanical, and optical characteristics of Sr3PX3 (X = Cl, Br) for enhanced optoelectronic application, Opt. Quant. Electron. 56 (2024) 1463, https://doi.org/10.1007/s11082-024-07388-2.

[20] M.A. Hossain, A.A. Sabi, H.A. Abdulhussein, A.A. Mousa, M.S. Abu-Jafar, R. K. Pingak, A.H.A. Nasria, W.H. Hassan, N.F.A. Mohammad, A. Hosen, Insights into the pressure-dependent physical properties of cubic Ca3MF3 (M = As and Sb): First-principles calculations, Heliyon 10 (2024), https://doi.org/10.1016/j.heliyon.2024.e38898.

[21] M.A. Hossain, A. Hosen, H.A. Abdulhussein, A.A. Mousa, M.M. Hasan, I.A. Ovi, M. R. Islam, R.K. Pingak, M.S. Abu-Jafar, Investigation of the physical properties and pressure-induced band gap tuning of Sr3ZBr3 (Z = As, Sb) for optoelectronic and thermoelectric applications: A DFT - GGA and mBJ studies, Results Eng. (2024) 103340, https://doi.org/10.1016/j.rineng.2024.103340.

[22] A. Algahtani, F. Rehman, M. Liaqat, N. Juraev, I. Khan, A.M. Alsuhaibani, V. Tirth, M.S. Refat, A. Zaman, Probing the physical properties of Sr3AsX3 (X= F and Br) perovskite compounds for prospective solar cell applications employing the DFT framework, Inorg. Chem. Commun. 162 (2024) 112186.

[23] A. Ghosh, M.F.I. Buian, N.L. Dey, M.S.I. Ria, A.A. Baki, A.A. Miazee, N.S. Awwad, R.I.C. Robin, H.A. Ibrahium, A comprehensive investigation of the Sr3AsX3 (X = F/Cl/Br) inorganic cubic perovskites' strain-induced structural, electronic, optical, and mechanical properties with solar cell applications, PCCP 26 (2024) 25890–25909, https://doi.org/10.1039/D4CP03286A.

[24] P. Giannozzi, S. Baroni, N. Bonini, M. Calandra, R. Car, C. Cavazzoni, D. Ceresoli, G.L. Chiarotti, M. Cococcioni, I. Dabo, A.D. Corso, S. de Gironcoli, S. Fabris, G. Fratesi, R. Gebauer, U. Gerstmann, C. Gougoussis, A. Kokalj, M. Lazzeri, L. Martin-Samos, N. Marzari, F. Mauri, R. Mazzarello, S. Paolini, A. Pasquarello, L. Paulatto, C. Sbraccia, S. Scandolo, G. Sclauzero, A.P. Seitsonen, A. Smogunov, P. Umari, R.M. Wentzcovitch, QUANTUM ESPRESSO: a modular and open-source software project for quantum simulations of materials, J. Phys. Condens. Matter 21 (2009) 395502, https://doi.org/10.1088/0953-8984/21/39/395502.

[25] W. Kohn, L.J. Sham, Self-consistent equations including exchange and correlation effects, PhysRev. 140 (1965) A1133–A1138, https://doi.org/10.1103/PhysRev.140.A1133.

[26] J.P. Perdew, A. Ruzsinszky, G.I. Csonka, O.A. Vydrov, G.E. Scuseria, L. A. Constantin, X. Zhou, K. Burke, Generalized gradient approximation for solids and their surfaces, PhysRevLett. 100 (2008) 136406, https://doi.org/10.1103/PhysRevLett.100.136406.

[27] K.F. Garrity, J.W. Bennett, K.M. Rabe, D. Vanderbilt, Pseudopotentials for high-throughput DFT calculations, Comput. Mater. Sci 81 (2014) 446–452, https://doi.org/10.1016/j.commatsci.2013.08.053.

[28] G. Kresse, J. Hafner, Norm-conserving and ultrasoft pseudopotentials for first-row and transition elements, J. Phys. Condens. Matter 6 (1994) 8245.

[29] J.D. Head, M.C. Zerner, A Broyden—Fletcher—Goldfarb—Shanno optimization procedure for molecular geometries, Chem. Phys. Lett. 122 (1985) 264–270.

[30] P. Blaha, K. Schwarz, G.K. Madsen, D. Kvasnicka, J. Luitz, wien2k, Augment. Plane wave local orbitals program calc, Cryst. Prop. 60 (2001).
[31] F. Tran, P. Blaha, Accurate band gaps of semiconductors and insulators with a semilocal exchange-correlation potential, PhysRevLett. 102 (2009) 226401, https://doi.org/10.1103/PhysRevLett.102.226401.
[32] K. Momma, F. Izumi, VESTA: a three-dimensional visualization system for electronic and structural analysis, J. Appl. Cryst. 41 (2008) 653–658.
[33] R. Gaillac, P. Pullumbi, F.-X. Coudert, ELATE: an open-source online application for analysis and visualization of elastic tensors, J. Phys. Condens. Matter 28 (2016) 275201.
[34] F. Karsch, A. Patkos, P. Petreczky, Screened perturbation theory, Phys. Lett. B 401 (1997) 69–73.
[35] P.W. Langhoff, S.T. Epstein, M. Karplus, Aspects of time-dependent perturbation theory, RevModPhys. 44 (1972) 602–644, https://doi.org/10.1103/RevModPhys.44.602.
[36] A. Otero-De-La-Roza, D. Abbasi-Pérez, V. Luaña, Gibbs2: A new version of the quasiharmonic model code. II. Models for solid-state thermodynamics, features and implementation, Comput. Phys. Commun. 182 (2011) 2232–2248.
[37] G.K. Madsen, D.J. Singh, BoltzTraP. A code for calculating band-structure dependent quantities, Comput. Phys. Commun. 175 (2006) 67–71.
[38] H.-J. Feng, Q. Zhang, Predicting efficiencies >25% A3MX3 photovoltaic materials and Cu ion implantation modification, Appl. Phys. Lett. 118 (2021) 111902, https://doi.org/10.1063/5.0039936.
[39] V.M. Goldschmidt, Die Gesetze der Krystallochemie, Naturwissenschaften 14 (1926) 477–485, https://doi.org/10.1007/BF01507527.
[40] C.J. Bartel, C. Sutton, B.R. Goldsmith, R. Ouyang, C.B. Musgrave, L.M. Ghiringhelli, M. Scheffler, New tolerance factor to predict the stability of perovskite oxides and halides, Sci. Adv. 5 (2019) eaav0693, https://doi.org/10.1126/sciadv.aav0693.
[41] K.M. Hossain, S.K. Mitro, S.A. Moon, M.M. Ali, S. Chandra, M.A. Hossain, Influence of heavy Hf doping in CeO2: prediction on various physical properties, Results Phys. 37 (2022) 105569.
[42] A.A. Emery, C. Wolverton, High-throughput DFT calculations of formation energy, stability and oxygen vacancy formation energy of ABO3 perovskites, Sci. Data 4 (2017) 1–10.
[43] A. Jehan, M. Husain, V. Tirth, A. Algahtani, M. Uzair, N. Rahman, A. Khan, S. N. Khan, Investigation of the structural, electronic, mechanical, and optical properties of NaXCl 3 (X= Be, Mg) using density functional theory, RSC Adv. 13 (2023) 28395–28406.
[44] S.A. Khattak, M. Abohashrh, I. Ahmad, M. Husain, I. Ullah, S. Zulfiqar, G. Rooh, N. Rahman, G. Khan, T. Khan, M. Salman Khan, S.K. Shah, V. Tirth, Investigation of structural, mechanical, optoelectronic, and thermoelectric properties of BaXF3 (X = Co, Ir) fluoro-perovskites: promising materials for optoelectronic and thermoelectric applications, ACS Omega 8 (2023) 5274–5284, https://doi.org/10.1021/acsomega.2c05845.
[45] O. Kabi, M.S. Abu-Jafar, M. Farout, A.A. Mousa, A. Bouhemadou, N. Erum, S. M. Azar, A. Bassalat, H. Abualrob, A.Y. Thabaineh, R. Khenata, Ab initio investigation of the structural, elastic, dynamic, electronic, and magnetic properties of cubic perovskite CeCrO3, ACS Omega 9 (2024) 11820–11828, https://doi.org/10.1021/acsomega.3c09292.
[46] M.A. Bezzerrouk, M. Hassan, R. Baghdad, S. Reguieg, M. Bousmaha, B. Kharroubi, B. Bouhafs, Thermodynamic, structural and electronic, properties of SnO2: By GGA and GGA + trans-blaha-modified Becke–Johnson (TB-mBJ) calculation, Superlattice. Microst. 84 (2015) 80–90, https://doi.org/10.1016/j.spmi.2015.02.046.
[47] A. Hosen, M.A. Hossain, M.S. Abu-Jafar, R.K. Pingak, A.A. Mousa, Unraveling lead-free Fr-based perovskites FrQCl3 (Q = Ca, Sr) and their pressure induced physical properties: DFT analysis for advancing optoelectronic performance, J. Phys. Chem. Solid 193 (2024) 112211, https://doi.org/10.1016/j.jpcs.2024.112211.
[48] S.S.A. Gillani, R. Ahmad, I. Zeba, M. Shakil, M. Rizwan, M. Rafique, M. Sarfraz, S. S. Hassan, Effect of external pressure on the structural stability, electronic structure, band gap engineering and optical properties of LiNbO3: an ab-initio calculation, Mater. Today Commun. 23 (2020) 100919.
[49] I.A. Ovi, M.R.R. Hasan, I.A. Apon, F. Zahra, The structural, magnetic, optoelectronic, and mechanical characteristics of NaGeX3 perovskites under pressure for solar-cell applications, Mater. Res. Express (2024) https://iopscience.iop.org/article/10.1088/2053-1591/ad594d/meta (accessed August 19, 2024).
[50] N.A. Noor, M. Hassan, M. Rashid, S.M. Alay-e-Abbas, A. Laref, Systematic study of elastic, electronic, optical and thermoelectric properties of cubic BiBO3 and BiAlO3 compounds at different pressure by using ab-initio calculations, Mater. Res. Bull. 97 (2018) 436–443, https://doi.org/10.1016/j.materresbull.2017.09.039.
[51] M.H. Miah, N.-E. Ashrafi, M.B. Rahman, M. Nur-E-Alam, M.A. Islam, K.A. Naseer, M.Y. Hanfi, H. Osman, M.U. Khandaker, First-principles study of the structural, mechanical, electronic, optical, and elastic properties of non-toxic XGeBr3 (X = K, Rb, and Cs) perovskite for optoelectronic and radiation sensing applications, Mater. Chem. Phys. 319 (2024) 129377, https://doi.org/10.1016/j.matchemphys.2024.129377.
[52] F. Litimein, R. Khenata, A. Bouhemadou, Y. Al-Douri, S.B. Omran, First-principle calculations to investigate the elastic and thermodynamic properties of R BRh_3 (R = Sc, Y and La) perovskite compounds, Mol. Phys. 110 (2012) 121–128, https://doi.org/10.1080/00268976.2011.635607.
[53] F. Mouhat, F.-X. Coudert, Necessary and sufficient elastic stability conditions in various crystal systems, PhysRevB 90 (2014) 224104, https://doi.org/10.1103/PhysRevB.90.224104.
[54] M.I. Naher, S.H. Naqib, Structural, elastic, electronic, bonding, and optical properties of topological CaSn3 semimetal, J. Alloy. Compd. 829 (2020) 154509, https://doi.org/10.1016/j.jallcom.2020.154509.
[55] M. Al-Fahdi, A. Rodriguez, T. Ouyang, M. Hu, High-throughput computation of new carbon allotropes with diverse hybridization and ultrahigh hardness, Crystals 11 (2021) 783.
[56] R. Hill, The elastic behaviour of a crystalline aggregate, Proc. Phys. Soc. Sect. A 65 (1952) 349.
[57] X. Diao, Y. Diao, Y. Tang, G. Zhao, Q. Gu, Y. Xie, Y. Shi, P. Zhu, L. Zhang, High-throughput screening of stable and efficient double inorganic halide perovskite materials by DFT, Sci. Rep. 12 (2022) 12633, https://doi.org/10.1038/s41598-022-16221-3.
[58] S.F. Pugh, XCII. Relations between the elastic moduli and the plastic properties of polycrystalline pure metals, Lond. Edinb. Dublin Philos. Mag. J. Sci. 45 (1954) 823–843, https://doi.org/10.1080/14786440808520496.
[59] A. Bouhemadou, R. Khenata, M. Kharoubi, T. Seddik, A.H. Reshak, Y. Al-Douri, FP-APW+ lo calculations of the elastic properties in zinc-blende III-P compounds under pressure effects, Comput. Mater. Sci. 45 (2009) 474–479.
[60] V. Tvergaard, J.W. Hutchinson, Microcracking in ceramics induced by thermal expansion or elastic anisotropy, J. Am. Ceram. Soc. 71 (1988) 157–166, https://doi.org/10.1111/j.1151-2916.1988.tb05022.x.
[61] L. Kleinman, Deformation potentials in silicon. I. Uniaxial strain, PhysRev. 128 (1962) 2614–2621, https://doi.org/10.1103/PhysRev.128.2614.
[62] L. Dong, S. Sun, Z. Deng, W. Li, F. Wei, Y. Qi, Y. Li, X. Li, P. Lu, U. Ramamurty, Elastic properties and thermal expansion of lead-free halide double perovskite Cs2AgBiBr6, Comput. Mater. Sci 141 (2018) 49–58.
[63] L. Qi, Y. Jin, Y. Zhao, X. Yang, H. Zhao, P. Han, The structural, elastic, electronic properties and Debye temperature of Ni3Mo under pressure from first-principles, J. Alloy. Compd. 621 (2015) 383–388.
[64] O.L. Anderson, A simplified method for calculating the Debye temperature from elastic constants, J. Phys. Chem. Solid 24 (1963) 909–917.
[65] M.E. Fine, L.D. Brown, H.L. Marcus, Elastic constants versus melting temperature in metals, Scr. Metall. 18 (1984) 951–956.
[66] D.R. Penn, Wave-number-dependent dielectric function of semiconductors, PhysRev. 128 (1962) 2093–2097, https://doi.org/10.1103/PhysRev.128.2093.
[67] L.-K. Gao, Y.-L. Tang, X.-F. Diao, First-principles study on the photoelectric properties of CsGeI3 under hydrostatic pressure, Appl. Sci. 10 (2020) 5055.
[68] S.Z.A. Shah, S. Niaz, T. Nasir, J. Sifuna, First principles insight into band gap tuning in bismuth based double perovskites X2NaBiCl6 (X= Cs, Rb, K) for enhanced optoelectronic and thermoelectric properties, Results Chem. 5 (2023) 100828.
[69] G. Yu, C.H. Lee, A.J. Heeger, S.-W. Cheong, Photoconductivity and optical conductivity in lightly doped Nd2CuO4- δ,, Phys. C Supercond. 203 (1992) 419–425.
[70] M.N. Islam, M.A. Hadi, J. Podder, Influence of Ni doping in a lead-halide and a lead-free halide perovskites for optoelectronic applications, AIP Adv. 9 (2019) 125321, https://doi.org/10.1063/1.5132985.
[71] M. Roknuzzaman, K. Ostrikov, H. Wang, A. Du, T. Tesfamichael, Towards lead-free perovskite photovoltaics and optoelectronics by ab-initio simulations, Sci. Rep. 7 (2017) 14025.
[72] A.B. Kuzmenko, Kramers–Kronig constrained variational analysis of optical spectra, Rev. Sci. Instrum. 76 (2005) 083108, https://doi.org/10.1063/1.1979470.
[73] S.A. Khandy, D.C. Gupta, Magneto-electronic, mechanical, thermoelectric and thermodynamic properties of ductile perovskite Ba2SmNbO6, Mater. Chem. Phys. 239 (2020) 121983.
[74] F. Peng, H.-Z. Fu, X.-L. Cheng, First-principles calculations of thermodynamic properties of TiB2 at high pressure, Phys. B Condens. Matter 400 (2007) 83–87.
[75] S.A. Mir, S. Yousuf, D.C. Gupta, First principle study of mechanical stability, magneto-electronic and thermodynamic properties of double perovskites: A2MgWO6 (A = Ca, Sr), Mater. Sci. Eng. B 250 (2019) 114434.
[76] S.A. Khandy, D.C. Gupta, Analysing cation-modified magnetic perovskites A 2 SnFeO 6 (A = Ca, Ba): a DFT study, RSC Adv. 11 (2021) 27499–27511.
[77] S. Yousuf, D.C. Gupta, Thermoelectric response of ZrNiSn and ZrNiPb Half-Heuslers: Applicability of semi-classical Boltzmann transport theory, Results Phys. 12 (2019) 1382–1386.
[78] R. Ullah, M.A. Ali, G. Murtaza, A. Mahmood, S.M. Ramay, The significance of anti-fluorite Cs_2NBI_6 via its structural, electronic, magnetic, optical and thermoelectric properties, Int. J. Energy Res. 44 (2020) 10179–10191, https://doi.org/10.1002/er.5638.

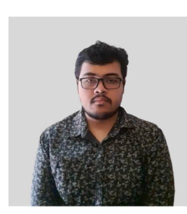

Muneef Hasan A dedicated researcher specializing in computational materials science focused on developing innovative materials for optoelectronics and energy applications. Earned a B.Sc. in Materials Science and Engineering from Khulna University of Engineering & Technology (KUET), with expertise in using advanced simulation tools to explore the physical properties of various compounds. Committed to driving advancements in material design to address challenges in energy efficiency and sustainability.

Adil Hossain A dedicated researcher with a background in Materials Science and Engineering, specializing in computational materials science. Research focuses on developing novel materials for optoelectronic and energy applications, utilizing advanced techniques such as density functional theory (DFT) and other computational modeling tools. Throughout the academic journey, several contributions to published works on perovskites and related materials have been made, driven by a strong curiosity and a commitment to innovation. The goal is to further explore advanced materials, aiming to make a meaningful impact through continued research and collaboration.

Heider A. Abdulhussein Dr. Heider A Abdulhussein is a researcher, assistant professor, and master and doctoral supervisor at the University of Kufa in Iraq. His primary focus is on the theory and simulation of nanoclusters, nanoparticles, surfaces, solids, and biological molecules, utilizing state-of-the-art computational approaches such as global optimization search strategies, Density Functional Theory (DFT), and Molecular Dynamic (MD) Simulation methods. In 2019, Dr Abdulhussein graduated from the School of Chemistry at the University of Birmingham in the United Kingdom, completing his PhD under the supervision of Professor Roy Johnston. In August 2019, Dr. Abdulhussein assumed the role of a lecturer in the Department of Chemistry within the Computational Chemistry Research group at the University of Kufa. Additionally, in November 2019, he was appointed as Administrator for the International Rankings Unit of the university. His career progressed steadily, and in May 2021, he was promoted to Assistant Professor of Physical Chemistry. Between 2021 and 2023, he engaged in various short-term research visits to the Faculty of Information Technology and Bionics at Pázmány Péter Catholic University in Hungary. As of July 2023, he joined the Faculty of Information Technology and Bionics at Pázmány Péter Catholic University to pursue postdoctoral research within the Structural Bioinformatics Research Group led by Professor Zoltán Gáspári. Since September 2024, he has become Head of the Department of Chemistry at the University of Kufa.

Abdullah Al Shadi A passionate researcher focusing on computational simulation, concentrating on the development of novel materials for optoelectronic and energy applications. Completed B.Sc. in Electrical and Electronic Engineering (EEE) from Khulna University of Engineering & Technology (KUET), emphasizing in the application of modern simulation techniques to investigate the physical properties of diverse substances. Dedicated to advancing material design for solving issues regarding energy efficiency and sustainability.

Bijoy Sorker With a B.Sc. in Electrical and Electronic Engineering (EEE), the focus has been on advancing knowledge in computational science and exploring the electronic, optical, and transport properties of materials. Research interests include developing simulation models to understand and enhance the performance of materials for optoelectronic and photovoltaic applications. Skilled in using tools like Quantum ESPRESSO, and Materials Studio, and committed to contributing to the future of energy-efficient technologies through innovative computational research.

Ahmed Adnan AL-Khafagi Ahmed Adnan Al-Khafagi is a Doctor of Philosophy in Analytical Chemistry at Al-Mustaqbal University College, Iraq. His research interests focus on general chemistry, analytical chemistry, flow injection analysis, and spectroscopy. Dr. Al-Khafagi has contributed significantly to the field of analytical chemistry, exploring advanced methods and techniques to improve the precision and efficiency of chemical analyses.He is known for his work on flow injection analysis and the use of spectroscopy in chemical studies. His expertise has garnered attention within the academic community, and he continues to mentor and collaborate with students and fellow researchers.

Redi Kristian Pingak Redi Kristian Pingak is a physicist specializing in quantum mechanics, computational materials, and condensed matter theory. He is currently pursuing his PhD at the University of Melbourne, Australia, and is affiliated with Universitas Nusa Cendana in Indonesia. Redi holds a Master of Science (MSc) from the University of Melbourne, which has greatly contributed to his expertise in advanced computational methods and theoretical physics.His research focuses on quantum mechanics and materials science, where he uses computational techniques to investigate the properties of materials at the atomic level.

Diana Dahliah Dr. Diana Dahliah is a researcher and assistant professor at An-Najah National University, Nablus, Palestine, with expertise in condensed matter and nanosciences. She is currently a visiting researcher at the Institute of Condensed Matter and Nanosciences at the Université Catholique de Louvain (UCLouvain) in Belgium, where she continues her research in the field of physics.Dr. Dahliah earned her Ph.D. from UCLouvain in 2021, after completing her Master's degree in physics at Miami University in Ohio, USA, where she graduated with a perfect score of 4/4 in 2012. She also holds a Bachelor's degree in pure physics from An-Najah University, with a high distinction score of 96.4%, obtained in 2010.Her professional journey began as a teaching assistant at Miami University from 2011 to 2012. Upon returning to An-Najah University, she worked as a lecturer in the physics department from 2012 until 2018, after which she pursued her doctoral studies in Belgium. In 2022, she was appointed as an assistant professor at An-Najah University.Dr. Dahliah's technical expertise spans across programming languages such as Python and C++, as well as proficiency in operating systems like Windows, Unix, and Linux. She is fluent in both English and Arabic, with excellent skills in reading, writing, and speaking both languages.

Mohammed S. Abu-Jafar Prof. Dr. Mohammed Abu-Jafar was born in Jenin city in 1960 and got his Tawjihi in Jenin secondary school in 1978. He obtained his BSc. degree in physics from An-Najah N. University in 1982. He got his MSc. in Physics from Jordan University in 1985. He is appointed to the physics department in An-Najah N. University in Jan. 1985. He achieved his PhD degree in Physics from Southern Illinois University (S.I.U.) at Carbondale-U.S.A. in 1991. He has been awarded a teaching assistant during his master and PhD studies in Jordan University and S.I.U. He is promoted to Associated Professor in Jan. 2002. He was a Chairman of Physics Department between 2001-2003. He was also a chairman of graduate studies for natural sciences between 2004-2007. He was the Dean of the Faculty of Graduate Studies between 2008-2014. He spent his sabbatical leave as a Postdoc at La Sapienza university, Rome, Italy in 2015 for one year. Twenty-seven master & PhD students have graduated under his supervision. Four conferences have been held under his supervision too. His research of interest currently is related to computational condensed matter physics using FP-LAPW method (WIEN2k code). Prof. Abu-Jafar has published more than 70 papers in a well-known international journals. He has constructed an E-Learning undergraduate course in classical mechanics. He is cooperative with many international journals as a reviewer.

Asif Hosen Asif Hosen, born on February 5, 1999, in Bangladesh, is a researcher in materials science and a lecturer at the Department of Materials Science and Engineering (MSE) at Khulna University of Engineering & Technology (KUET), Bangladesh. He completed his Bachelor of Science (BSc) in Materials Science and Engineering (MSE) at KUET in 2023. His research is focused on innovations and advancements in materials science.